2019-01-01

Impact Of Temperature And Screw Speed On Material Meso-Structure And Tensile Strength In Large Area Pellet-Fed Additive Manufacturing

Xavier Jimenez Guzman
University of Texas at El Paso, xjimenezgu@miners.utep.edu

IMPACT OF TEMPERATURE AND SCREW SPEED ON MATERIAL MESO-STRUCTURE AND TENSILE STRENGTH IN LARGE AREA PELLET-FED ADDITIVE MANUFACTURING

XAVIER ANDRES JIMENEZ GUZMAN, B.S.M.E

Master's Program in Mechanical Engineering

APPROVED:

David Espalin, Ph.D., Chair

Ryan Wicker, Ph.D.

Amit Lopes, Ph.D.

Charles Ambler, Ph.D.
Dean of the Graduate School

Dedication

This thesis is dedicated to my parents, Xavier and Enmita, and my sister Maria Belen who always encouraged and supported my education

IMPACT OF TEMPERATURE AND SCREW SPEED ON MATERIAL MESO-STRUCTURE AND TENSILE STRENGTH IN LARGE AREA PELLET-FED ADDITIVE MANUFACTURING

by

XAVIER ANDRES JIMENEZ GUZMAN, B.S.M.E

THESIS

Presented to the Faculty of the Graduate School of

The University of Texas at El Paso

in Partial Fulfillment

of the Requirements

for the Degree of

MASTER OF SCIENCE

Department of Mechanical Engineering

THE UNIVERSITY OF TEXAS AT EL PASO

May, 2019

Acknowledgements

I want to thank my advisor and mentor Dr. David Espalin for all the guidance and encouragement during my master studies at UTEP. I want to thank Dr. Ryan Wicker for providing me the opportunity to conduct research at the W.M Keck Center for 3D Innovation, a cutting-edge additive manufacturing research facility, established by him in 2001.

During my time at UTEP, I had the pleasure to work with many brilliant students some of which deserve my recognition for this work. I would like to thank Mr. Jose Motta and Mr. Chris Minjares for their help with machine design and machining; Mr. Eduardo Meraz Trejo, Mr. Fernando Rodriguez, Mr. Kevin Schnittker and Mr. Leonardo Gutierrez for their help with specimen preparation; Dr. Edel Arrieta for his help with digital image correlation, Mr. Luis Ochoa for mold design and manufacturing, Mr. Jose Luis Coronel for his help with technical writing and Mr. Kazi Billah for his technical contribution to this work. I would like to thank Dr. Calvin Stewart for allowing us to use his digital image correlation system.

I would also like to thank Mr. Steve Thaporn, Mr. Bobby Baer and all the team at Cincinnati Incorporated for their support during integration of the wire embedding tool. I would like to thank George Roberts from Autodesk for the help with developing the CAM post.

Finally, I would like to thank my parents, Xavier and Enmita, who always encouraged me to further my education. It is because of them that I have been able to achieve this master's degree. I want to thank my sister Maria Belen and the rest of my family for all the encouragement I always receive. I also want to thank my girlfriend Abigail Fernandes for her support and understanding through my master's degree.

This research was performed through the National Center for Defense Manufacturing and Machining under the America Makes Program entitled "Multi-Functional BAAM: Big Area Additive Manufacturing w/ Multi-Purpose Wire Embedding" and is based on research sponsored by Air Force Research Laboratory under agreement number FA8650-12-2-7230. The U.S. Government is authorized to reproduce and distribute reprints for Government purposes

notwithstanding any copyright notation thereon. The views and conclusions contained in this document are those of the author and should not be interpreted as necessarily representing the official policies, either expressed or implied, of the Government.

Abstract

Evolution in additive manufacturing, specifically in material extrusion, has resulted in large-scale machines capable of extruding thermoplastic-matrix composite materials in higher volumes to fabricate products for large-scale applications. As with small- and medium-scale material extrusion, the properties of the final product often correlate directly with the bevy of print parameters employed. The current research was performed to evaluate the effects of the screw speed and temperature on an ABS 20%wt. carbon fiber thermoplastic processed on a Big Area Additive Manufacturing (BAAM, Cincinnati Inc) machine. Five screw speeds (50, 150, 250, 350 and 400 rpm) and three extruder temperature profiles were selected (one profile based on manufacturer recommendations, and two profiles outside the recommendations wherein one was above and the other was below the recommended temperatures). For extruded and printed beads, qualitative and quantitative results are reported for void percentage, tensile strength, yield strength, modulus, mass loss due to off-gassing, specific gravity, and surface roughness. At lower screw speeds, small voids were identified throughout the entire radius of the specimens. This voids are the result of volatile off gassing or material degradation. At screw speeds of 250 rpm or more, larger voids were identified at the edges of the specimens. These voids are significantly larger than gas voids and are caused by air which is introduced due to the speed at which material is entering the barrel of the extruder. Results highlighted the need to understand and model internal voids in beads, as gas voids are not eliminated through the printing process. Although the use of higher temperatures allowed for an increased extruder output, they also resulted in a higher void content, also assumed to be a result of increased off-gassing. Overall, findings from this work can be used in academic and applied research in the area of large-scale additive manufacturing. This document also contains a section describing the controls for a non-standard CNC tool with a wire embedder end effector that was mounted into the BAAM system. This tool allows for the introduction of 3D printed electronics at large scale which in the past has only been reserved for small scale additive manufacturing systems.

Table of Contents

List of Tables

List of Figures

Chapter 1: Introduction

1.1 BACKGROUND

Additive manufacturing (AM), also known as 3D printing, is a manufacturing process where goods are created by adding layer-upon-layer of material. In the late 1980s, the first AM systems entered and revolutionized the market with the ability to create parts directly from a computer-aided design (CAD) model. The advantages of AM include but are not limited to the ability to customize and produce complex parts otherwise impossible to achieve with traditional manufacturing, shorter lead times, less waste and minimized number of parts. As the AM process only puts material where is needed instead of taking material away (i.e., subtractive manufacturing), the process produces less material waste. Because there is no need for specialized custom tooling, changing the CAD file or adding complexity into the part does not substantially increase its cost. Furthermore, the lead times are shorter as no parts have to be pre-ordered to start the print process. As an example, printing a complicated assembly with multiple parts combined into one could be less expensive than printing an entirely solid block, as the weight (or material consumption) is the primary driver of the cost.

AM disadvantages include high production costs, slow build rates, necessary design expertise, lack of economy of scale, post-processing and poor mechanical properties. AM material systems are very specialized pieces of equipment that require high-quality material to operate which leads to high production costs. The layer-by-layer manufacturing process which is achieved through a variety of different methods yields slow built rates. These built rates with the additional time required for post-processing of parts does not allow for AM to benefit from the economy of scales. Moreover, although some systems (i.e., desktop material extrusion) have a low learning curve, other AM systems require experienced engineers and operators due to the complexity of design and process parameters (i.e., Hybrid AM systems). Finally, for many AM processes, parts have a poor mechanical response when compared to their traditional counterpart (material extrusion desktop systems versus injection molding). Overall, it can be said that AM should not

be the manufacturing process of choice for all parts, but there are many cases where AM can leverage those advantages and produce high-quality products at a lower cost.

One of the most common used AM system is material extrusion, in which material (usually filament) is pushed through a heated nozzle mounted on a gantry that allows the material to be deposited on the flat X-Y plane. Once a layer is complete, the gantry can move up in the Z-axis to create the rest of the 3-dimensional object (Turner *et al.* 2014). The majority of these systems have a build envelope of less than 1-meter cube, because of the slow deposition rate inherent with using material in the form of filament. To fill this gap, in 2014, Oak Ridge National Labs in partnership with Cincinnati Inc. developed the Big Area Additive Manufacturing (BAAM) machine. As with smaller material extrusion systems, the BAAM heats thermoplastic material to a flowable state that is then deposited by a gantry to create 3D parts. Instead of using a heated nozzle to heat filament, the BAAM system has a single screw pellet extruder which heats pellet feedstock at higher rates if compared to desktop material extrusion systems. Although the technology is commercially available and able to produce large scale parts, work is needed in several areas including, the influence of process parameters on mechanical properties of materials and parts, modeling of the process, in-situ process monitoring and more. The thesis work presented here will focus on the impact that process parameters have on printed material quality and the mechanical response of BAAM parts.

In traditional manufacturing, multi-functional components are created in a series of steps using several processes. When creating new products, time to market (TTM) is an important measure to quantify success and profitability. The need for multiple steps, processes and specialized tooling reduces the TTM, which can result in less profit or a compromised opportunity. Similarly, when parts need to be created to perform as tooling for the manufacturing of more complex products, the production time needs to be optimal as not to slow manufacturing. Moreover, because traditional manufacturing requires the use of multiple processes, the parts need to be transferred across different groups within a single company. The use of 3D printing

technology coupled with electrical interconnect placement can reduce production time and cost for low volume high-value applications.

Modified stereolithography (SL) and fused deposition modeling (FDM) systems integrated with micro-dispensing or wire embedding technology can create 3D parts with electrical interconnect and components. The wire placement technology, also called wire embedding technology, uses either thermal energy or ultrasonic energy to embed not only solid wires but also metal foil. Wire embedding has been used to create different parts including embedded RF antennas, CubeSat modules, and a microwave path antenna (Lopes *et al.* 2014; Espalin *et al.* 2014; Shemelva *et al.* 2015). The biggest challenge with transferring wire embedding technology into a large-scale setting is the low deposition rate achieved with it. A method for high deposition of wire was developed through the adaptation of tungsten inert gas welding to avoid slowing down the printing process, (Espalin, David. 2014). This thesis work will also focus on the control implementation of a wire embedding tool into the Big Area Additive Manufacturing (BAAM) machine.

1.2 MOTIVATION

Just as with traditional material extrusion, the shape and quality of the part rely on process parameters, such as printing temperature profile, traversing speeds and extruder output. Consequently, the user has access to a large number of process variables; however, there is not a full understanding of the effect that those parameters have on part quality. The work presented in this thesis will fill a knowledge gap in the large-scale AM community.

New tools need to be developed to add hybrid capabilities to this system to accommodate the large-scale nature of BAAM. For wiring placement, a tool with a high wire deposition speed must be developed as not to compromise the printing speed of the BAAM. Furthermore, the wire gauge must be large enough to accommodate high power applications as larger components are able to be placed on BAAM parts.

During the AM design process, many considerations are taken to create a product that meets the goal and needs of the user. As outlined in ASTM 52910, the design requirements include product usage considerations, business considerations, geometry considerations, material property considerations, process specific considerations, communication considerations, and product-specific considerations. In terms of material property considerations, it is essential to know certain behaviors and characteristics of the as-printed material and of a final part. Those considerations include mechanical properties, thermal properties, and electrical properties, between others. The mechanical properties must be measured in different loading conditions including, tensile, flexural, impact, compression, shear, fatigue and creep states. Due to large area pellet extrusion being a new technology, there is a lack of information regarding these properties which limits the use of this technology in many applications.

1.3 THESIS OBJECTIVES

There were five thesis objectives as listed below:

1. Develop the mechatronic design of a custom wire placement tool into the BAAM machine.
2. Design and developed a method of communicating with the tool to transfer wire placement information.
3. Experimentally determine the effects that extruder screw speed and temperature settings have on material properties.
4. Experimentally determine the mechanical behavior that ABS 20%wt carbon fibers have under static loading.

1.4 THESIS OUTLINE

The rest of the thesis was divided into 6 chapters. Chapter 2 is composed of an overview of the BAAM printing process and literature review of topics pertinent to this thesis. These topics include anisotropic properties of material extrusion parts, static mechanical properties, cyclic mechanical properties, void formation, rheology and thermal properties, digital image correlation,

and wire embedding technologies. In Chapter 3, the wire placement tool for the BAAM system is described. Chapter 4 consists of the experimental methodology used to obtain the void content, surface roughness and microscopy images of extruded and printed beads. Additionally, this chapter will also describe the methodology to obtain the mechanical properties of the material under static loading. Chapter 5 is going to be a discussion of the experimental results. Finally, conclusions are offered in Chapter 6.

Chapter 2: Literature Review

2.1 INTRODUCTION

Additive Manufacturing (AM), as defined by the American Society for Testing and Materials, is the process of joining materials to make parts from 3D model data, usually layer upon layer, as opposed to subtractive manufacturing and formative manufacturing methodologies (ISO/ASTM52900-15, 2015). The first set of patents were filed in 1984 by both French and U.S inventors, but it was only Chuck Hull of 3D Systems Corporation (US Patent No. 4575330A, 1986), who finished the process and was granted the patent for his stereolithography process (SLA). Nowadays, there are 7 main types of AM including binder jetting, directed energy deposition, material extrusion, material jetting, powder bed fusion, sheet lamination, and vat photopolymerization. Independent of the specific process, there are 6 main steps employed in fabricating a part; 1-Computer Aid Design Model (CAD), 2-converting the part into a file with additive manufacturing format (AMF) or stereolithography format (STL), 3- 'slicing' the part in layers and creating the machine commands, 4-importing instructions to the AM machine, 5-Start the building process and 6-post-process the part.

AM parts were first developed to be used as prototypes due to the ease of manufacturing and simplicity to make design changes in comparison to traditional prototyping methods. Now, because of the improvement in mechanical properties, end-use parts are currently being manufactured using different AM processes. For example, the Naval Air Systems Command (NAVAIR), stated that they believe nearly 1,000 3D printed parts will be approved for fleet use by the end of 2018 (Saunders, 2018). Similarly, Oak Ridge National Labs in collaboration with Sandia National labs developed an additive manufactured wind turbine blade mold (Sandia National Lab, 2018). Correspondingly, newer and larger printers are being developed to accommodate the new demand for AM parts. For example, GE is developing the world largest metal 3D printer, which would have a 1-meter cube building envelope (GE Reports, 2017).

2.2 MATERIAL EXTRUSION ADDITIVE MANUFACTURING

Although the main focus of this thesis is large-scale material extrusion AM, the author would like to explain the basics of Fused Deposition Modeling (FDM), as this is the most common method of material extrusion (Figure 1). In FDM, the material is drawn through a heated nozzle and deposited while the dispensing head moves along the X, Y, and Z coordinates as to create 3D models in a layer by layer fashion (US Patent No. 5121329A, 1992). With the expiration of this patent, a large number of desktop printers were developed, as well as industrial grade and do-it-yourself (DIY) style ones. This led to a significant drop in price which increased the sale of printers to a level never seen since the creation of this technology (Rundle, 2014). Since many of the newer printers also come with an easy-to-use software package, it was not only the financial limitation but the learning curve that also disappeared.

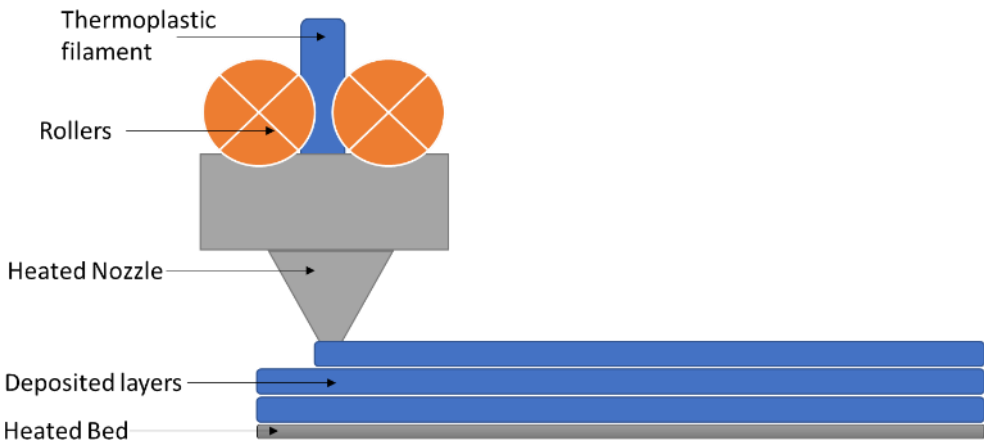

Figure 1: Fused Deposition Modeling schematic (FDM)

The development of new materials and industrial grade AM systems allowed for end-use parts to be produced for different fields including aerospace, automotive, consumer products, dental, education and medical. Some applications require larger parts that could not be produced even in one of the largest commercially available FDM systems, the Fortus 900mc, with a build volume of $0.72m^3$.

In recent years, efforts from government and industry have focused on developing different large-scale AM systems for different materials including; concrete, thermoplastics, and metal. For example, companies like XtreeE and BetAbram are working on developing large-scale concrete printers with a build envelope large enough to print a small house (74 m^2) (Murphy, M., 2019). In 2014, Oak Ridge National Labs (ORNL) and Cincinnati incorporated introduced the first ever large-scale material extrusion printer in the world, the Big Area Additive Manufacturing machine (BAAM). This machine is able to print up to 40 kg of thermoplastic material per hour, which is about 250 times faster than any traditional material extrusion system. A similar system called Large Scale Additive manufacturing (LSAM) was developed by ThermWood corporation. This machine combines both material extrusion and 5-axis machining into one system.

In March of 2016, Ingersoll machine tools Inc. and ORNL partnered to develop the largest thermoplastic extrusion 3D printer to date named Wide and High Additive Manufacturing (WHAM) machine (Love, L; *et al*. 2017). The machine, completed in the Fall of 2018, has a build envelope of 7 x 14 x 3 m (23' x 46' x 10') and an extruder with the ability to deposit 70 kg/hr of thermoplastic material (3D printing media network. 2018). Similarly, to the LSAM, the WHAM machine is also able to exchange the extruder for a 5-axis milling machine for finishing operations.

2.3 BIG AREA ADDITIVE MANUFACTURING

The Big Area Additive Manufacturing (BAAM) machine was developed by Oak Ridge National Lab (ORNL) and is commercialized by Cincinnati Incorporated. The largest version of the system has a printing volume of 6 x 2.28 x 1.82 m (240''x 90'' x 72'') and a maximum extruder output of 45 kg/h. The BAAM system consists of several sub-systems as seen in Figure 2, one being a material dryer, which dries the pellet material from 0.2% water content to 0.05% or less, to avoid having air bubbles inside the final printed part due to entrapped moisture. The dryer has a material bin able to carry 450 pounds of material which acts as the BAAM material reservoir. There is an open loop vacuum system that takes material from the reservoir to the gantry located inside the machine. The 3-axis XYZ gantry houses a smaller material reservoir, the extruder, and

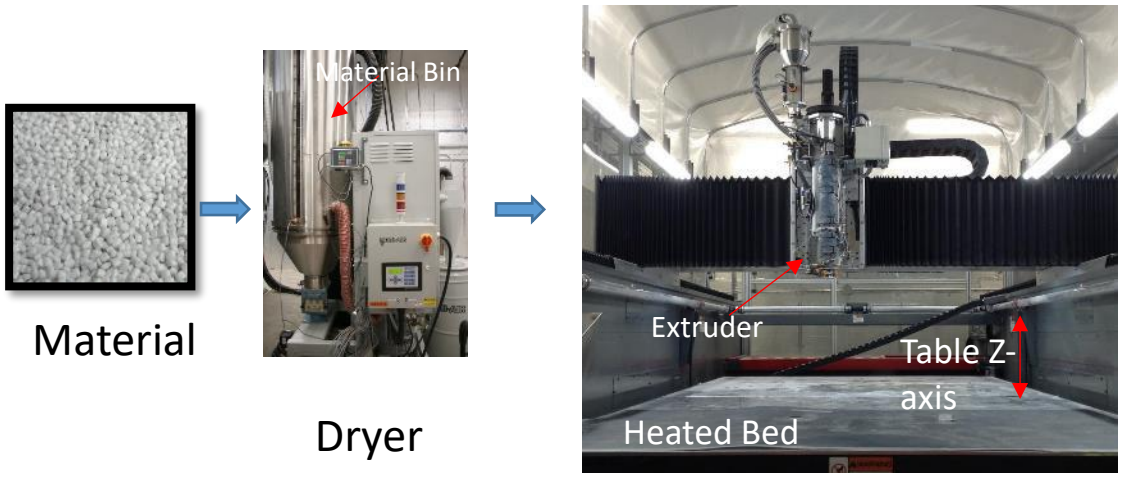

Figure 2: BAAM system material process

other electrical components. Material only travels to the gantry when a sensor in the small material reservoir requests it, as having material outside the dryer and exposed to the ambient humidity for long periods of time is detrimental to the moisture content.

The printer was designed to work with thermoplastic pellets which are consistently pushed down the nozzle by a single screw and melted by a set of 5 heaters as seen in Figure 3. This process is very similar to the standard non-AM plastic extrusion which has been widely used for the last 80+ years (US patent # US2567960A). The use of thermoplastic pellets not only allows for the large print speed but it also reduces the cost of the material by a factor of 10. From market prices, a 1 lb spool of ABS20%wt carbon fiber material is ~50 dollars, while the same weight of pellets is only ~ 5 dollars. At the exit of the nozzle, a tamper mechanism flattens the extruded material to aid in the reduction of voids and to keep the bead dimensions consistent.

As defined before, the third step of the additive manufacturing process chain is to slice the Standard Tessellation Language (STL) to create machine commands. The slicer used for the BAAM was developed by ORNL at the manufacturing demonstration facility in Knoxville, TN. The slicer is able to control all parameters of the machine except the extruder and bed temperature

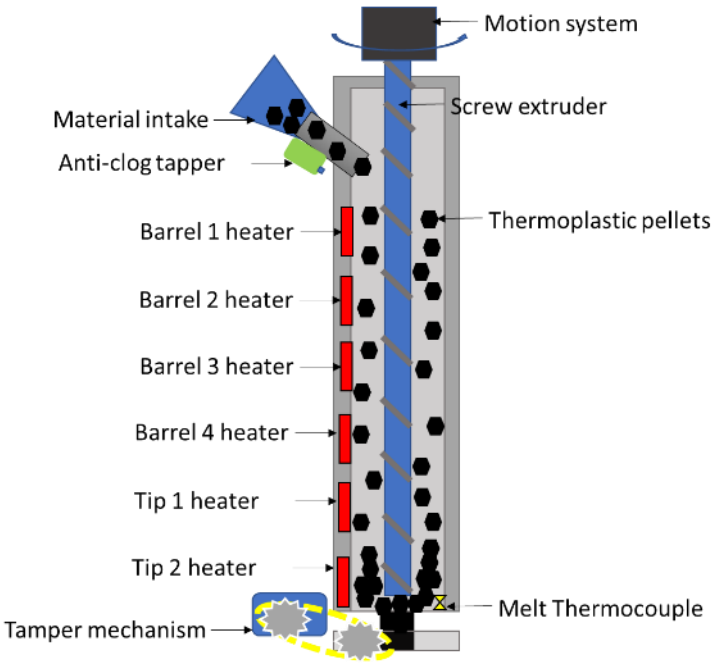

Figure 3: BAAM extrusion system

settings that are controlled through the human machine interaction (HMI). Just as it occurs with other systems, BAAM offers a large number of machine-specific settings within its slicer which are listed in **Error! Reference source not found.**.

The extruder temperature is controlled from the BAAM computer where the user is able to set the temperature for 6 heaters up to 400 °C. The temperature settings are usually obtained from the material manufacturer data sheet, and if that information is not available, the material parameters can be obtained through a combination of thermal-mechanical tests which will be covered in a later chapter (Ajinjeru, C. *et al.* 2016). Similarly, the temperature for the 8 heaters on the bed can be controlled from the HMI, with a maximum bed temperature of 200°C. It should be noted that for printing operations, a metal mesh material is placed first on the build platform (or bed), then an ABS sheet is secured on top using a cloth tape to seal the edges. A vacuum system outfitted into the bed is used to secure the ABS sheet flat against the bed. Due to the thermal resistance, the ABS sheet is never able to achieve the set temperature for the bed (Compton, B. *et al.* 2017).

Table 1: List of parameters and control mechanism for the BAAM system

Extruder temperature	HMI BAAM Software
Bed Temperature	HMI BAAM Software
Frequency of Tamper	Slicer
Purging conditions	Slicer
Extruder feedrate	Slicer
Smoothing	Slicer
Infill Settings	Slicer
Layer time	Slicer
Acceleration of the gantry	Slicer
Skins Settings	Slicer
Inset Setting	Slicer
Line removal (minimum feature size)	Slicer
Presence of a canopy	External
Material Drying	External

The deposition rate of the printer (kg/hr of material) is influenced by the extruder output and the temperature profile chosen in the HMI, therefore, in order to determine the correct parameters, experimental procedures are needed. The machine is set to purge for a determined amount of time, and then the weight of the extrudate is measured. This information and a set of input parameters are fed into the ORNL flow calculator tool which determines the extruder output (rpm), and traverse speed (in/s) needed. The parameters are deposition rate, bead height, bead width and type of material being used.

2.4 MECHANICAL PROPERTIES

Just as with other additive manufacturing processes, BAAM parts have a high anisotropic behavior due to the layer by layer printing process (Ahn, S. *et al.* 2002). Because this thesis is focused on filled materials, it is essential to understand the effect that fibers have on mechanical behavior. Love *et al.* studied the influence that chopped fiber reinforcement has on the thermal conductivity, strength, stiffness, and part distortion. The authors selected four different desktop printers and their proprietary blends of ABS to create five sets of ASTM D638 type V specimens oriented in the XYZ direction and the Z direction. Although the results were very positive for the

XYZ direction where the strength and stiffness increased by ~200% and 400% respectively, the Z-direction strength was reduced by ~50%. Similar behavior was identified by Zhong *et al.* (2001), but no explanation is given for this behavior.

As additive manufactured parts behave differently from parts created using traditional methods (e.g. Injection molding or plastic extrusion), standards must be developed to correctly characterized material properties. Furthermore, because large scale parts contain bigger beads, the test specimens fabricated following ASTM D638 would not capture enough beads of material within the cross section where stresses are concentrated. In addition, the size of voids and prints defects is much larger for large scale extrusion systems than for FDM ones. For example, an ASTM D638 type I specimen with a gauge area of 91 mm^2 fabricated with FDM technology has about ~700 beads. If the same specimen was created from a BAAM part, the number of beads would be reduced to ~3 beads. Duty *et al.* presents a modified version of a type I specimen to be used when characterizing large scale AM materials. A modified specimen manufactured with BAAM would contain 38 beads which are still lower than the FDM specimen, but still provides an insight on the behavior of BAAM parts.

2.4.3 Static properties

Initial characterization of BAAM manufactured material was presented by Duty *et al*. (2015). Modified type I specimens were printed using 20% GF-ABS, 40% GF-ABS, 15% CF-ABS, 20% CF-ABS and 20% CF-PEI. The temperature settings were maintained constant for every material, and two extrusion rates were used, 4.5 and 16 kg/h. Although this paper provides mechanical properties for multiple materials, the authors mentioned the lack of control and optimization given to the printing parameters of BAAM. Additionally, extrusion rates are meager in comparison to the max capacity of the BAAM. Parts printed using ABS 20%wt. carbon fibers on the XZY direction were found to have a strength of ~60 MPa while the injection molded specimens of ~40MPa. The ZXY samples showed strength values of ~8MPa, which as mentioned before, shows the high degree of anisotropy that filled thermoplastic composites have. This paper

did not present any strain data, which impedes obtaining other properties that should be considered in the engineering design process.

Schnittker *et al.* used digital image correlation (DIC) to characterize the mechanical properties of ABS20%wt. glass fiber (Schnittker *et al*. 2019). The concept of using DIC to obtain specific mechanical properties will be analyzed in a further section; in this section, the objective is to understand the mechanical behavior of the BAAM parts. In this paper, the authors conducted tensile tests using the modified type I specimens, where the average UTS was found to be 52.8 MPa. This value is about 14 MPa lower than the results obtained by Duty *et al.* (2015), which is attributed to the printing parameter not being optimized for the hexagonal structure. In this paper, the authors tried to mirror the parameters used by Duty *et al.* which might have caused the part to have larger voids or the layer temperature to be too low for proper adhesion (Compton *et al.* 2017). Neck layer size was measured for two samples which determined that there was a minimal variation of this value between samples. This indicates that the tensile strength is uniform along the specimen, which was confirmed from the small variation between the tensile test results. Although the deviation between samples was low, the void size was large which contributed to the low mechanical performance. This thesis will present work using a similar approach to test the static mechanical properties of ABS20%wt. carbon fiber.

2.4.4 Void formation

Duty *et al.* performed microscopy imaging on the cross-section of BAAM printed parts and found the presence of voids within a bead of material. The authors believe that the presence of voids is due to entrapped air inside the pellets or the off-gassing of volatiles due to incorrect processing conditions within the BAAM extruder. The BAAM was outfitted with a new extruder and screw to mitigate this effect. Authors also found than filled ABS was prone to have a higher void content than neat ABS. In literature, the presence of voids in short fiber reinforced thermoplastics is well documented. Those voids, even in small number, can significantly decrease the mechanical strength of the material. The interlaminar strength of the material can decrease by

7% for each 1% of voids up to a total void content of 4% (Narkis *et al.* 1989). Narkis *et al.* manufactured test coupons using both injection molding and plastic extrusion (not AM) technology and then analyzed the void content of them. The samples were fabricated from Noryl, which is an amorphous blend of polypropylene oxide, with 10%wt., 20%wt. and 30%wt. of glass fibers. They used a single screw extruder with a screw speed of 50 rpm and a temperature profile of 260/270/280°C. The void content of the samples was measured using a pycnometer following ASTM 792-66 and images were taken on polished specimens using reflected light microscopy. The extruded samples showed an increasing void content with increasing fiber content both from the density values and the imaging, which in fact confirms that the voids were not created by the polishing of the samples. It should be noted that voids were found in unfilled specimens which indicates that void formation is not only dependent on fiber loading. The injection molding specimens showed significantly smaller voids which are attributed to the cooling process occurring under pressure. Authors mentioned that fiber debonding from the matrix and the cooling process affects the void content. Upon cooling, external surfaces solidify first, thus impeding the contraction of the inner section of the bead. A substantial temperature effect is present in void formation with void content increasing as temperature increases. The slower solidification of the material and the decreased viscosity and pressure at higher temperatures are the leading causes for that behavior. Increasing the feedrate also seems to increase the voids content as air might get entrapped within the material thus increasing the void content. It was also mentioned that voids could be caused by other factors including moisture, volatiles evolved during cure and residual solvents. Additionality, Narkis *et al*. found that voids might also play a role in surface roughness, as voids might push fibers to different locations.

During testing of the first BAAM prototype, Duty *et al.* noted the presence of voids between beads of material. This behavior has also been identified in the FDM process (Huang, B., & Singamneni, S. 2015). The bonding between beads can be characterized by the neck created between two adjacent beads (Francis, V., & Jain, P. K. (2016); N. Turner, B, *et al*. 2014). Viscosity and surface tension are the two main factor driving the neck size, thus, affecting the bond between

beads. It should be noted that this work is referring to side-to-side contact of the bead and is not characterizing the bond strength of layers deposited on top of one another. The addition of fibers into ABS plastic increase the viscosity and surface tension of the material (Schnittker *et al*. 2019) thus, creating larger voids. Duty *et al.* performed scanning electron microscopy on printed samples using neat-ABS, glass fiber-ABS, and carbon fiber-ABS. It was discovered that the filled materials had a smaller neck length (i.e., larger voids between beads). The BAAM was then outfitted with a tamper mechanism, to compact each deposited bead within the immediate surroundings. Although this reduced porosity and improved inter-layer bonding, the tamper was not able to eliminate the voids. The need for a flattening mechanism was also identified by Thermwood Corp, who installed a roller system on the LSAM machine.

2.4.5 Fatigue properties

To accurately design for the BAAM system, cyclic loading tests are needed to determine the fatigue life of parts. The cyclic response of FDM parts manufactured using different unfilled materials like ABS and PLA is well documented in the literature (Lee, J., Huang, A. 2013*;* Ziemian, C. *et al.* 2014). Lee mentions in his paper the ease of access to static material properties for multiple AM materials but the lack of any cyclic loading study. This paper presents one of the first studies into the fatigue response of ABS printed using FDM technology. In this paper, Lee and Huang printed dog-bone specimens in multiple orientations using both ABS and ABSplus on a Stratasys Dimension. First, static tensile tests were performed to determine the UTS of the samples in each orientation. The cyclic loading tests were performed at 80, 60 and 40 percent of the UTS for 10,000 cycles. For longer run cycles, the test was restarted and appended to avoid a problem with the amount of data being stored. It is mentioned how micro-voids and air gaps can negatively affect the print, and the authors provide some techniques to reduce their occurrence. Due to print defects and weak bonds between material beads, the specimens did not rupture at the gauge length. This study presented the first look into cyclic loading, but due to printing inconsistencies and sample size, the results only show a trend and are not conclusive about the

behavior of ABS under fatigue loading. Also, the authors did not discuss the frequency used during testing and did not monitor the temperature to check for hysteresis.

Ziemian *et al.* (2014) also focuses on the fatigue properties of ABS and mentions Lee and Huang's challenges and shortcomings. Dog-bone specimens were fabricated on a Stratasys Vantage-i using ABS-P400 (Stratasys Ltd. Eden Prairie, MN US) following ASTM D638. Four printing orientations were used in this study; 1-longitudinal or 0°, 2-diagonal or 45°, 3-transverse or 90°, and 5- +45°/-45°. Injection molded specimens were also fabricated using the same material. In this work, each sample included 4 specimens. Tensile tests were performed to determine the UTS of the specimens following ASTM D638. For the cyclic loading, the specimens were tested at 90, 75, 60 and 45 percent of the UTS. Authors used a stress ratio of 0.1 which is widely used for fatigue tests of polymers. Following ASTM D7791, fatigue testing was performed at a frequency of 0.25 Hz to avoid a loss of mechanical properties due to hysteresis and a max cycle life of 17,500. Results indicated that the ultimate and yield strengths are the largest for the longitudinal, followed by +/-45, diagonal and transverse. Interestingly, the +/-45 samples had the most extended fatigue life followed by the longitudinal direction, diagonal and transverse. The orientations were the beads (or roads) were aligned to the testing direction yielded better results as the polymer chains are running in that direction. The higher life cycle for the +/-45 was surprising for the authors, and they could not provide an explanation for it. The biggest challenge for Ziemian *et al.* was that some of the specimens did not fail before the test max cycles limit, which prevented the authors from commenting about the fatigue life of ABS at certain orientations.

Cyclic loading of thermoplastic material can yield a hysteresis loop in the strain-stress curve indicating that part of the strain is not recovered during the cycle (Rittel, D. 2000). Most of the lost energy is converted into heat as a function of the strain and strain rate (Mason, J. *et al.* 1994). Rittel found that Polycarbonate will heat up during cyclic testing and the temperature rise is dependent on cyclic frequency and the applied stress level. While the ASTM 7791 does not state the allowed temperature variation, while other authors stated the temperature increase should not go over 2 degrees (Mandell, J. *et al.* 1981). It should be noted that this work was performed for

small Type I and V ASTM D638 specimens, the author believes that the larger modified specimens will not be as susceptible to a temperature increase.

The challenge that some researchers have encountered is that running experiments at a low frequency (0.25 to 1 Hz) for long cycles is computationally expensive regarding memory needed. Some fatigue papers set the maximum number of cycles to 10,000 or less, and others increase the frequency to 5 Hz in order to test higher life cycles (Afrose, M.F. *et al.* 2016*;* Fischer, M., Schöppner, V. 2017). The low frequency is preferred to avoid increasing the temperature within the part which can compromise the mechanical properties of the material (Ziemian, S. *et al*. 2014) The lower frequency might allow the tensile tester to reach the set values of stress or strain keeping the controller's feedback error to a minimum. Finally, the different frequencies and loads will activate the different mode of failure within the specimen, so the final application of the part is the man driver at dictating the frequency to be used (Local motors insight). In this thesis, the effect that frequency has on temperature during cyclic loading is explored, as a higher frequency is preferred to achieve longer life cycles.

In the case of reinforced thermoplastic composites printed using AM, the literature is very scarce. Although there is some work being performed on continuous fiber reinforcement using the FDM process (Agarwal *et al.* 2018; Goh *et al.* 2018), there is a lack of published work in reference to short fiber reinforced thermoplastics. Currently, there is only one conference paper focused on the fatigue behavior of large-scale thermoplastic materials (Hill, C. *et al.,* 2016). Hill et al produced the same modified type I specimen being used in this thesis using the prototype version of the BAAM system. Tensile, flexural and fatigue tests were performed on ABS 20%wt. carbon fiber but the number of specimens used for fatigue does not allow to generalize the behavior of this material (1 specimen per stress level). Moreover, the paper does not present a stress-strain curve or mention the yield point of the material. Without this information, some of the specimens could have been tested over the yield strength which would cause a premature failure under cyclic loading due to hysteresis. Overall, the paper presents an initial look at the behavior that large-scale thermoplastic materials have under cyclic loading.

Although AM materials behave differently than traditionally manufactured reinforced composites, some of the knowledge build in that area can be transferred to AM. The fatigue behavior of short fiber reinforced composites is complicated due to the vast number of failure mechanism that can occur; fiber fracture, matrix cracking, matrix crazing, fiber buckling, fiber-matrix interference failure and delamination (Nouri *et al.* 2009). These mechanisms can occur independently or at the same time, which can create problems when determining the cause of failure. Also, the failure mechanism is not going to be the same at different stress levels (Degrieck & Paepegem, W. 2001). Added to all these factors, is the inherent anisotropy and increased void content present in thermoplastic printed using large scale systems.

2.5 RHEOLOGY AND THERMAL PROPERTIES

Polymers are usually described based on their crystallinity, either as amorphous, crystalline, or semi-crystalline polymers. Amorphous polymers are materials in which the polymers chains are not in any given order which gives the material a glass-like behavior. Examples of amorphous polymers include acrylonitrile butadiene styrene (ABS), polycarbonate (PC) and polyetherimide (PEI). On the contrary, the molecules in crystalline polymers are arranged in a specific pattern, where polymer chains are locked in place next to the other. However, in reality, crystalline polymers also have an amorphous behavior present when connecting one or more crystals. Due to this behavior, this type of polymers is referred to as semi-crystalline. Examples of semi-crystalline polymers include Nylon (PA), Polyaryletherketone (PEEK), and Polyphenylene sulfide (PPS).

Both semi-crystalline and amorphous polymers are used in material extrusion additive manufacturing. Printing with amorphous polymers is better because these materials retain their shape after extrusion due to their glassy-like behavior. In contrast, semi-crystalline materials shrink during the crystallization process which decreases the ability of the material to retain the shape after extrusion. ABS is one of the most common polymers for the material extrusion process, and it will be the focus of this thesis, as all the specimens will be produced using this material. In

the FDM process, the thermoplastic extrusion occurs inside an oven to reduce part warpage. The effect called warpage occurs when a large temperature gradient is present across the part, which leads to deformations within the part. The deformation not only creates inaccurate geometries but it can also hinder the manufacturing process by releasing the part form the print platform or causing the nozzle assembly to crash against the part. Because the BAAM deposition does not occur within a heated enclosure, Duty *et al.* observed warping issues when printing neat ABS. In order to avoid this and to add strength to the part, chopped fibers were added into the materials which resulted in no warping for low-temperature materials and reduced warping for high-temperature ones. As a result, most BAAM materials have fillers in the form of chopped fibers. Because pellet extrusion additive manufacturing uses traditional pellet feedstock, the availability of material is quite large. Table 2 shows the different matrix materials and fillers available in the market according to a leading material manufacturer (Sabic. Houston, TX US).

To determine necessary processing conditions for the pelletized thermoplastic feedstock, it is necessary to perform a thermal and rheological analysis (Ajinjeru, C. *et al.* 2017). Although currently, this process is not well defined in the literature, the following contains a possible method to characterize these materials. The process starts by testing the material via thermogravimetric

Table 2: List of materials and fillers available for pellet extrusion additive manufacturing

Thermoplastic Matrix	**Fillers**
ABS	Carbon fibers
PC, PC/ABS, PC/PBT	Glass fibers
PEI	Minerals
PSU	Flame retardants
PA11	Heat stabilizers
PES	UV agents
PPSU	Thermally conductive fillers
PEEK	
PPS	
PA6	
PA66	
PPA	
PPE, PPE/PA	

analysis (TGA) in order to determine the decomposition onset temperature (ODT), or the temperature where the material starts to decompose (ASTM E2550-17). TGA is a technique in which the mass of a specimen is measured as a function of temperature or time while being subjected to a controlled-temperature regimen (ASTM E473-18). At temperatures over the ODT, the material will off-gas volatiles, thus increasing the possibility of bubble and void formation as mentioned in the void formation section of this document. TGA can also be used to determine the rate at which volatiles are produced and to perform a compositional analysis (ASTM E1131; ASTM E2008).

The next step is to perform differential scanning calorimetry to determine the glass transition temperature (T_g) of the material (Schawe, J. 1995; ASTM E1356). The T_g denotes the midpoint of a temperature range over which an amorphous polymer is transformed from its glassy state, thus, making the material a viscous liquid (Forrest, J. *et al.* 2002). For semi-crystalline materials, it is possible to find the melting and crystallization temperature using a similar approach (ASTM E794). DSC can also determine the enthalpies of fusion and crystallization and the specific heat of a material (ASTM E793, ASTM E1269). The enthalpy measures the quantity of heat exchanged by the system and its surroundings as the fusion and crystallization process occurs. The specific heat of a material indicates the amount of energy required to heat a specified amount of material to a certain temperature. Using the information provided by the DSC, a minimum processing temperature can be obtained. The melt temperature is set to at least ~100 °C over the T_g, following a rule well established in other similar polymer processes like injection molding and plastic extrusion, (Ajinjeru, C. *et al.* 2016; Rauwendaal, C. 2019). Finally, a rheological analysis is performed to determine the viscoelastic properties of the material at different temperatures. Dynamic melt rheology is an analysis of the deformation that material has under applied stresses under certain processing conditions (Shenoy, A. 1999; ASTM D4440). The rheology study is able to provide the complex viscosity, the resistance to steady flow, as a function of frequency, strain amplitude, temperature and time. As it was seen in previous sections, the viscosity of a material affects the bonding between two adjacent beads of material. Additionally, the viscosity is also

related to the mechanical stability of the material. In other words, high viscosity can preclude the printing of another layer of material. Many users have observed this behavior, and it also captured in the literature (Roschli, *et al.* 2019).

Ajinjeru *et al*. (2016) characterized both neat ABS and ABS 20%wt. carbon fibers to determine the processing conditions for this material using the BAAM. The TGA experiments were conducted in air using a heating rate of 10°C/min up to 600 °C. The results yielded a DOT of 310 °C, without any influence by the carbon fibers. The DSC was conducted using a heating rate of 10°C/min from 25 °C to 450 °C. samples were cooled to 25 °C at a rate of 5 °C/min and then reheated for a second run. The results showed the T_g for ABS is independent on fiber loading and stayed constant at a value of 105 °C. Following the rule of thumb described before, the processing condition of ABS should be between 225 and 310. Authors picked 230 °C, 250 °C, and 270 °C to perform rheology measurements. Rheology measurements were taken on a parallel plate rheometer at a frequency range of 0.1-628 1/rad with an applied strain of 0.1%. Results show that ABS is shear thinning for all processing conditions. Shear thinning is defined as the effect when viscosity decreases with an increasing load (Mezger, T. 2006). The increase in temperature decreases the viscosity, and the addition of fibers decreases the viscosity. It was also shown that the shear thinning effect is enhanced by the carbon fibers.

2.6 Modeling Of Large-Scale Pellet Extrusion Additive Manufacturing

In additive manufacturing, modeling tools are valuable because they provide insight in terms of the thermal profile and residual stresses within the part. This information can be used to alter G-code or printing parameters to avoid print defects, warping or cracking. Additionally, being able to account for thermal shrinkage allows obtaining higher tolerances which reduce material waste and thus increases the profitability of the machine. Two pieces of software are currently available in the market to model the material extrusion AM process; Digi-mat and Genoa 3DP simulations. Digi-mat models the residual stresses and warpage on parts printed using fused filament fabrication (FFF). Genoa 3DP uses progressive element activation and local material

orientation to simulate both FFF and large-scale pellet extrusion systems. Talagani *et al.* (2015) used this software to model a car chassis printed on the BAAM system. Other models also include other material properties including thermoviscoelastic properties and polymer crystallization (if printing semi-crystalline materials) (Brenken *et al*. (2019).

One of the most critical factors that affect large scale systems is the large thermal gradients between the beads of the deposited material. This occurs because large scale systems do not have an enclosed heated envelope as FDM systems do, so the material is continually cooling down. Additionally, the large bead size and higher deposition rates also induce the appearance of thermal gradients even for simple geometries (Duty *et al.* 2015). Compton *et al.* present a 1-dimensional heat transfer model of one thin bead wall printed using the BAAM system (Figure 4). Three cases were developed in the model; top layer, middle layers or bottom layer. For the top layer, convection and radiation are considered out of three sides and conduction from the bottom. For the middle and bottom layers, the conduction is considered from the top and bottom sides. The difference with the bottom layer is that the bed is assumed to be at a constant temperature. The temperature within each bed is assumed to be the constant, which is realistic for this thin wall. For a complicated part, the model needs to be upgraded to 2D. Although some of the material properties are temperature

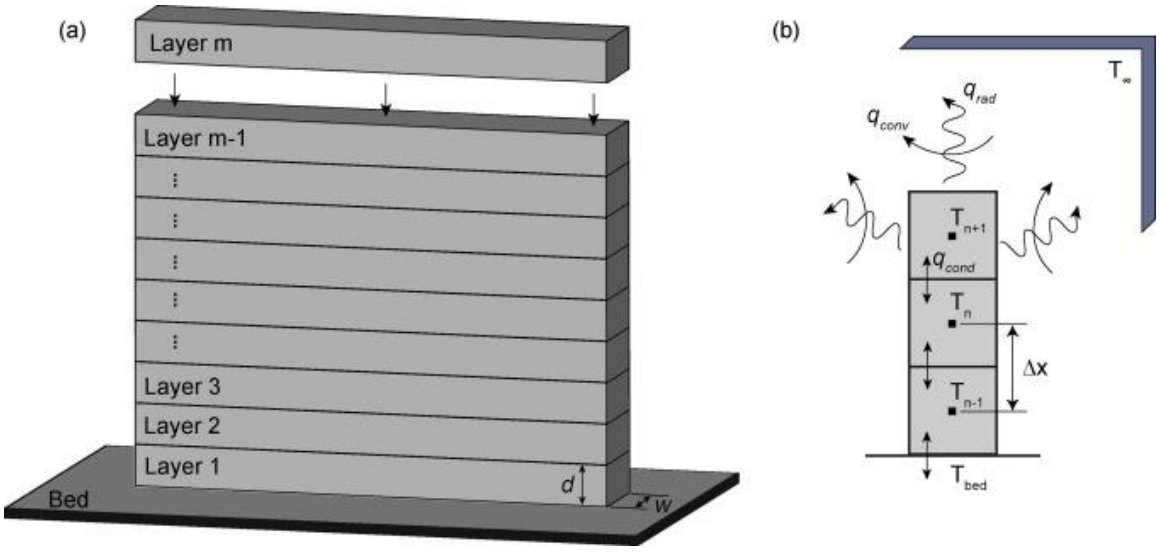

Figure 4: (a) 1D thermal model schematic showing geometry, and (b) boundary conditions developed by Compton *et al*. (2017)

dependent, for this study, they are considered constant. In this paper, Compton *et al.* concluded that the temperature of the previously printed bead prior to deposition of a new layer needs to be at least at T_g. Experiments have shown that when the temperature is under the T_g, cracking and warping can occur. To avoid this problem during the printing process to manufacture specimens for this thesis, the Compton model was used to confirm the layers were always over T_g before the deposition of the new layer.

2.7 DIGITAL IMAGE CORRELATION

Digital Image Correlation (DIC) involves tracking visible features on a specimen through the analysis of still images that are captured with digital cameras. The method has been used since the 1980s to measure full-field strain and displacement which allow bridging the gap between experiment and simulation (Hild and Foux, 2006). Schnittker *et al.* (2019) explain that the images are divided into groups containing a pattern or feature, and then each group is compared to a reference image. The tracking is achieved by comparing the change of grayscales levels at every N-number of pixels with each subset. Following the manufacturer recommendations, the system needs to be calibrated before measurements can be taken. An image with a grid of dots with known separation is used to correlate the physical distance and pixel distance of the dots. Virtual extensometers can be installed prior to testing, as it is typically done with real extensometers. The advantage of DIC is that new virtual extensometers and strain gauges can be added after the test. This allows capturing the mechanical behavior of the part even if the specimen does not break where it was expected. DIC also allows studying crack formation and propagation through the analysis of the full filed strain and displacement images. DIC has shown strain measurements within ±3% compared to clip extensometers (Arrieta *et al.* 2018).

2.8 WIRE EMBEDDING

A multi-functional component is defined as a part that has more than can serve for more than one purpose. For example, a satellite panel with embedded circuitry is both serving a mechanical (i.e., load bearing) and an electrical function. One approach to create multi-functional

components is using additive manufacturing (AM) to produce 3D printed electronics (parts with embedded circuitry). Many different AM technologies have been used to create 3D printed electronics, but stereolithography (SL) and fused deposition modeling (FDM) is the most relevant ones. Modified SL and FDM systems integrated with micro-dispensing or wire embedding technology can create 3D parts with electrical interconnects and components.

Micro-dispensing is a technology similar to AM, but instead of depositing AM material (i.e., material used to build the part) on a plane, it deposits conductive material on top of previously deposited AM material. Previous work involved using SL technology and micro-dispensing to create 3D electronics such as a gaming die or a three-axis magnetic flux sensor (Macdonald et al. 2014). The biggest challenge when using SL technology is the poor mechanical properties of the parts if compared to thermoplastic material (Espalin *et al.* 2014). Micro-dispensing systems have been adapted to FDM machines to create 3D printed electronics because they have better memchanical properties. Espalin *et al*. (2014) fabricated a CubeSat module using ULTEM 9085. Due to voids and cracks inherently present within FDM parts, inks tend to spread from the intended path (Perez and Williams, 2014).

The disadvantage of using micro-dispensing in both FDM and SL is that the conductive material within the part cannot be cured or sintered as it is traditionally done with PCB boards, because the thermoplastic or resin is not able to withstand the required high curing/sintering temperatures. A in situ laser curing system for silver-based conductive inks proved successful at curing only less viscous inks (Lopes, A., *et al.,* 2014). Overall, the resistivity of those traces was very high, which did not allow for the creation of parts with higher power applications. Due to this, efforts were made to developed a system to place solid wire onto the printed part (Espalin *et al.* 2014). The wire placement technology, also called wire embedding technology, uses either thermal energy or ultrasonic energy to embed not only solid wires but also metal foil. Wire embedding has been used to create different parts including embedded RF antennas and a microwave path antenna (Shemelya *et al.* 2015; Liang *et al.* 2015). This technology was transferred into a machine named the Multi3D system which combines multi-material FDM 3D printing,

micro-machining, component placement, and wire embedding. The multi-process is enabled by the implementation of material handling robotics and a heated portable platform (Coronel, 2015; Ambriz, 2015). When combining large area additive manufacturing systems with wire embedding, the placement of the wire needs to occur at high speed as to not slow down the printing process. Also, as described before, extended layer times leads to poor mechanical properties, cracking, warping or print failure. Ultrasonic energy is not well suited to be used with large diameter wire and a faster speed because the process is not able to transfer energy fast enough to achieve the required temperature increase in the wire (~250 °C). A method of heating the wire using a discharge arc developed by Espalin (2017), was found to be successful at providing the required temperature increase. The arc heating method and resistive heating were compared, concluding that the latest required higher power consumption. The arc heating approach is very similar to tungsten inert gas (TIG) welding. In this process, a non-consumable electrode made of tungsten is used to create an arc towards the metal part being welded. Similarly, this process was studied and optimized to heat the wire (acting as metal being welded) with the non-consumable electrode. Argon is used to shield the area to avoid contamination of the wire and electrode. Additionally, the gas also serves as a cooling agent for the torch. The wire arc heating system is comprised of different components including a power supply, torch (i.e., electrode), arc starter and a gas flow valve. From the control's perspective, the power supply needs to be controlled in order to adjust voltage and amperage parameters prior to and during wire embedding operations. The arc starter, used to provide the initial energy to create the arc, needs to be actuated at the beginning of every path. Finally, the gas valve open start the controlled flow of gas toward the torch.

Chapter 3: Mechatronic design and control implementation of wire embedder tool

3.1 PROJECT OVERVIEW AND DESIGN REQUIREMENTS

The project "Multi-Functional BAAM: Big Area Additive Manufacturing with multi-purpose wire embedding" was granted by America Makes, one of the institutes created by the

national network for manufacturing innovation, which focuses in accelerating the development of additive manufacturing (AM). Design requirements were defined to create a tool suitable for the BAAM system. The requirements were set as follows:

1. Increase the throughput of the wire embedding technology
2. Integrate wire embedding hardware with BAAM controller
3. Mechanically integrate the wire embedding tool on the BAAM machine
4. Identify CAM software for producing 5-axis, wire embedding G-code
5. Develop a CAD/CAM post processor to prepare BAAM G-code specific to wire embedding

The increase of throughput outlined in objective one is necessary because of the high printing speed that the BAAM possesses. Also, the diameter of the wire that can be embedded needs to be increased from previous tools to accommodate for high power applications (~1 mm diameter, 14-gauge wire). The speed of wire embedding used in smaller FDM systems is about 10 mm/s, and it has to be increased to 100 mm/s. Objective 2 and 3 outlines the process of integrating the new components into the current firmware of the machine both in terms of controls and mechanics. A piece of software will have to be identified to create five-axis instructions for the machine. Finally, a G-code post processor will serve to integrate the wire embedding and printing instructions.

3.2 Mechanical Design and Arc Welding

Previous methods that were used to embed interconnects into FDM parts were based on ultrasonic energy or micro-dispensing of conductive material. Solid wire must be used to achieve low resistivity within those interconnects, which negates the use of micro-dispensing. The problem with using ultrasonic energy relies on that with the larger diameter wire and a faster speed; the process is not able to transfer energy fast enough to achieve the required temperature increase in the wire (~250 °C). The next idea was to use heated air to provide energy to the wire to increase

its temperature before embedding it to the plastic. Experiments were performed, but this method was unable to provide the required energy to embed the wire.

A method of heating the wire using a discharge arc was found to be successful by providing the required temperature increase with a low current consumption if compared to resistive heating (Figure 5) (Espalin, D. 2017). The target material for the interconnects is copper (low resistivity), whose resistivity value is low enough to render resistive heating ineffective for this application. The selected arc heating approach is very similar to inert tungsten gas (TIG) welding. In this process, a non-consumable electrode made of tungsten is used to create an arc towards the metal part being welded. Similarly, this process was studied and optimized to heat the wire (i.e., metal being welded) with the non-consumable electrode. Argon is used to shield the area to avoid contamination of the wire and electrode. Additionally, the gas also serves as a cooling agent for the torch. The wire arc heating system is comprised of different components including a power supply, torch (i.e., electrode), arc starter and a gas flow valve. From the control's perspective, the power supply needs to be controlled in order to adjust voltage and amperage parameters prior to and during wire embedding operations. The arc starter, used to provide the initial energy to create the arc, needs to be actuated at the beginning of every path. Finally, the gas valve open starts the controlled flow of gas toward the torch.

Figure 5: Embedded wire into a BAAM printed part

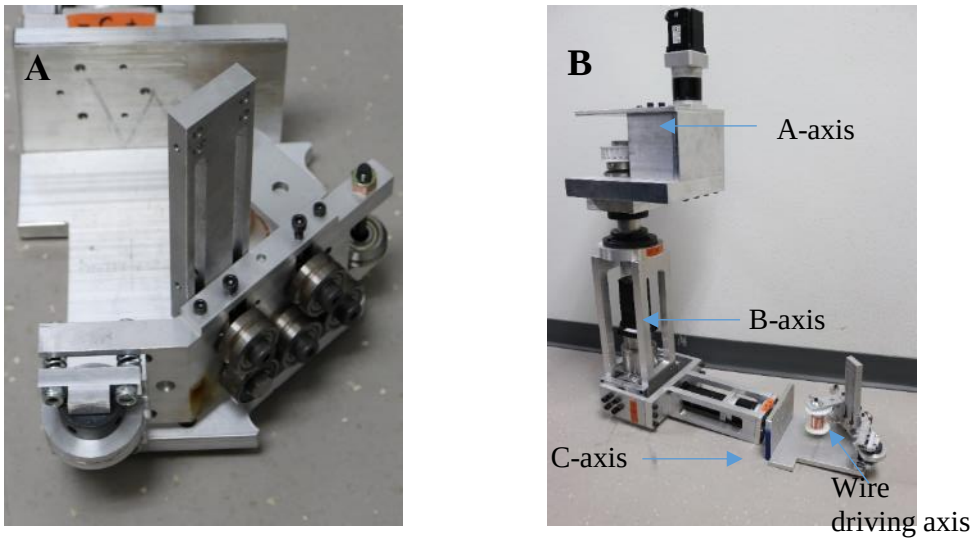

Figure 6: Wire embedder tool (A) and tool arm (B)

Up until this project, most of the efforts on wire embedding were centered on planar surfaces. For this project, the goal was to create a tool able to place wire on multi-axes surfaces (contoured and planar). This would allow for the wire to be placed during or after the printing process in any side of a part. To achieve this, the tool needed to have three axes (A, B, C and wire driving) which complemented with the X, Y and Z of the BAAM creates a 6 degree of freedom (DOF) non-standard robotic arm. The tool has two major components, the embedding tool (Figure 6-A) and the tool arm (Figure 6-B). The embedding tool houses the wire driving motor, sensors, wire spool, torch and application roller. The tool arm houses the rest of the motors and an electrical panel.

3.3 CONTROLS

Two strategies for controlling the tool and communicating with the BAAM system were devised. The first strategy was to have a separate programmable logic controller (PLC) that would control the tool axis based on commands sent by the BAAM's PLC. Using this approach would result in possible problems with synchronization and timing making the tool follow an incorrect path. The second alternative was to integrate all the new components into the BAAM's PLC (Figure 7). This was the chosen alternative due to the simplified integration and because Cincinnati Inc. would support this effort. The equipment selection, process development and G-code

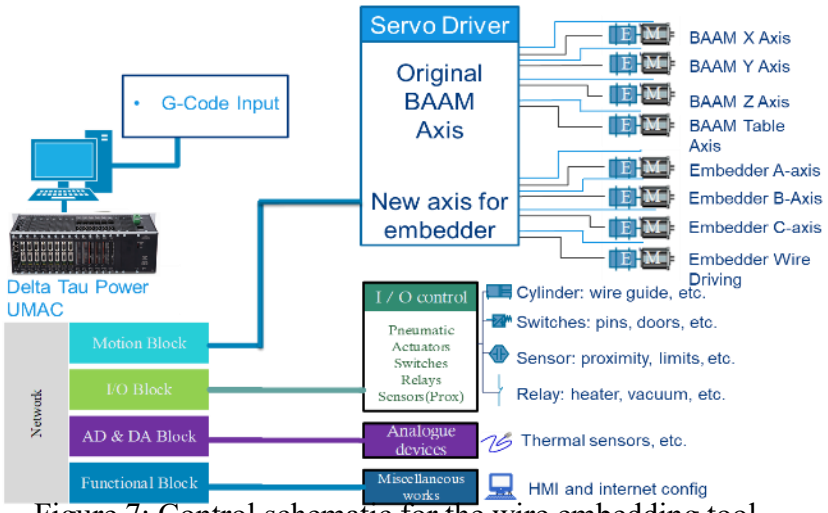

Figure 7: Control schematic for the wire embedding tool

development would be managed by UTEP, while Cincinnati Inc. would modify the machine's firmware, create new electrical panel for components and perform initial testing.

The first part of the control work is to understand all the different components and their control mode (Table 3). The table provides the name, function and control mode for each component. All the devices need to be controlled using G-code, a method of controlling a gantry system based on positions for all the motors. Also, G-code can transfer information to the machine via M-codes to control the additional components (i.e. power supply). Although there are some standard M-codes across multiple platforms, many of the M-codes are created from scratch and

Table 3: List of devices to be controlled

System	Device	Control
Embedder movement	Pneumatic actuator	M-code
	A-axis	G-code
	B-axis	G-code
	C-axis	G-code
Wire Driving	Wire driving axis	G-code
Arc Welding	Power Supply	M-code
	Arc starter	M-code
	Gas flow valve	M-code
Sensors	Before embedder pyrometer	M-code
	After embedder pyrometer	M-code
	Proximity sensor	M-code

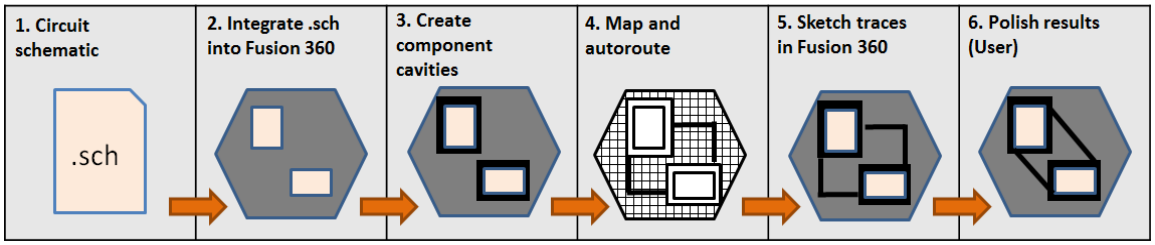

Figure 8: 3D routing software pipeline

are custom to a specific system. For this project, many codes were created to control all the different devices mentioned before. For example, some codes are used to provide voltage and amperage information to the machine or to turn the pneumatic actuator on.

3.4 G-CODE

The process for the creation of multi-functional components starts by designing the circuit in Autodesk Eagle software (Figure 8). The circuit is then exported from Eagle and imported into Fusion 360 using a modified and custom file developed during this project. The next step is for the user to design the component and move the components to the desired places. Then, the software is going to map the whole 2D surface where the wire needs to be placed and it will autoroute all connections. At this point, the information needs to be transferred to machine instructions for the manufacturing process to start.

Autodesk Fusion 360 offers a computer-aided manufacturing (CAM) environment, where the user can create instructions for computer numerical control (CNC) manufacturing. Fusion 360 supports different subtractive processes including but not limited to milling, turning and water jet cutting. The software can output information for machines with two, three, four and five axes. The CAM functionality can be modified to output machine instructions for wire placement through the use of a custom post. In a CAM software, a post adds all the specific commands needed to run a machine like the toolpaths, speeds and M-codes. A custom post was developed in partnership with Autodesk and Cincinnati Inc to obtain machine instructions for the BAAM tool.

2.5 WIRE EMBEDDING PROCESS

As it was explained in the previous section, the wire embedding process starts by creating G-code using Fusion 360. The code is then transferred into the BAAM system, where it read by the PLC. The process continues by starting the code using the BAAM, then the tools in the BAAM offset following G-code (Figure 9-B). Once the wire embedder is at the correct height, then the machine can move to the starting position (Figure 9-C). Then, the arc starts heating the wire while simultaneously beginning movement (Figure 9-D, E). Once the wire trace is completed, the tools move up to leave some wire protruding (To connect the components). Then wire stops moving while the arc heats the wire to the point that it breaks (-F). The final step is to push wire out of the tool and reset all controls to start another trace. Three sensors are placed on the tool: two pyrometers, and a proximity sensor. The pyrometers record information about the temperature of the plastic and wire before and after embedding. This is relevant information from a research perspective to make sure experimentation is always consistent. Similarly, the proximity sensor is used to record the distance away from the plastic that the tool is at. Because the roller in the tool has springs, the user could place the tool at different heights causing inconsistencies with experimentation. Currently, this tool has been fully implemented in a BAAM system at Cincinnati Inc headquarters and is awaiting further testing.

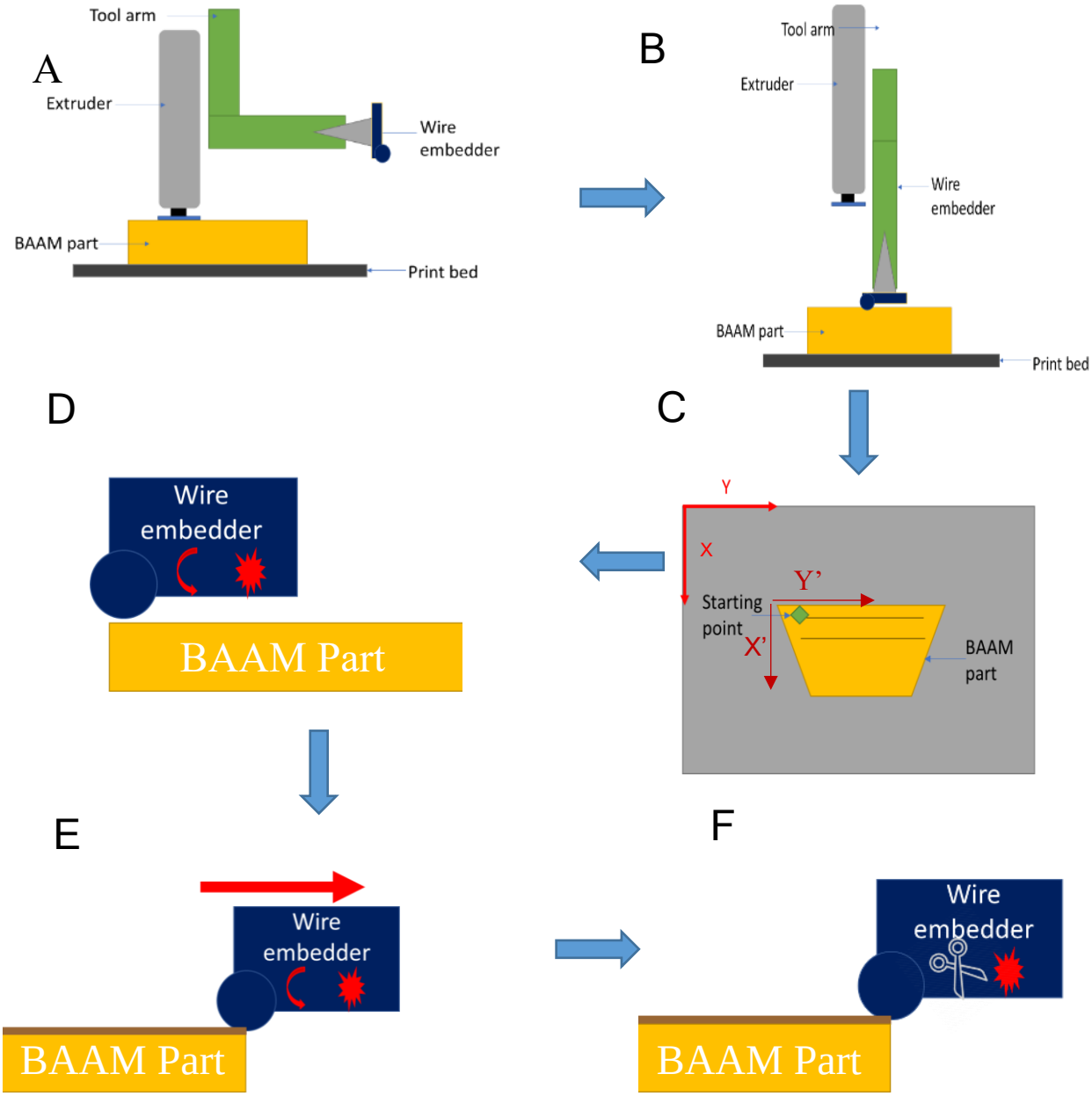

Figure 9: Wire embedding process; 1) Printing process is interrupted, 2) Offset BAAM tool, 3) move to starting position, 4) Start wire arc, and 5) Cut wire.

Chapter 4: Effect of temperature and screw speed on material meso-structure

4.1 Materials and Methods

4.1.1 Specimen Fabrication

The thermoplastic-matrix composite evaluated in this work was Electrafil J-1200 CF20 3DP (Techmer PM, Clinton, Tennessee, US): an ABS thermoplastic filled with 20% (by weight) carbon fiber. Prior to experimentation and printing, the material was dried following the manufacturer's recommendation of 4 hours at 80°C. It should be noted that previous experiments were conducted on material dried and printed on two different days, which resulted in high variance due to drying the same batch of material a second time for the second printing sequence. To mitigate this variance, data presented in this manuscript is from material dried and printed on the same day using a batch of material not previously dried.

In this paper, "extruded specimens" refers to beads extruded in air (i.e., not on the build platform) and collected directly from the nozzle, while "printed samples" are beads collected after printing a one-layer square (30cm x 30cm) on the 110°C heated build platform while using the tamper. Extruded specimens were produced by extruding material for 30 seconds and collecting the last 127 mm (5 in.) of the extruded bead, corresponding to approximately the last seconds of extrusion. This was done to remove the effects caused by tool traversing speed, platform temperature, decomposition of material already in the barrel for prolonged periods of time, and the physical change caused by the tamper.

Specimens were extruded and printed using varying temperature profiles and extruder screw speeds (50, 150, 250, 350, and 400 rpm) on a BAAM machine (Cincinnati Incorporated,

Table 4: Temperature profiles for extruded and printed specimens

		temperature (°C)						
		melt	barrel					
			1	2	3	4	5	6
manufacturer recommendation	upper limit	293	276	276	287	293	293	293
	lower limit	260	246	260	260	265	271	271
average temperature (AT)		276	255	268	276	282	279	276
minimum temperature (MinT)		204	190	204	204	210	215	215
maximum temperature (MaxT)		321	293	304	304	315	321	321

Harrison, Ohio, US). The screw speeds were chosen to cover the BAAM's extruder range (0-400 rpm). The temperature profiles were based on recommendations supplied by the material manufacturer (via material datasheet), which were offered as lower and upper temperature limits for each of the six heated zones in the extruder, as listed in Table 1. The average temperature (AT) profile was created using each zone's average recommended temperature. The minimum temperature (MinT) profile was offset below the manufacturer recommended lower limit. Since the manufacturer recommendations were delivered on the Fahrenheit scale, the MinT profile was offset by 100°F. The maximum temperature (MaxT) was offset above the upper limit by 50°F. Extrusion was also performed at 100°F above the recommended limit, but since the material's decomposition onset temperature (DOT) is 258°C (496°F), as measured by thermogravimetric analysis using a TGA55 (TA instruments, New Castle, DE US) according to ASTM E1131, material degradation prohibited proper testing. The DOT, defined as the temperature at which 1% mass loss occurs, has also been reported as 310°C (Ajinjeru, C, *et al.*). For the printed specimens, due to the various screw speeds and temperature profiles during printing, the tool traversing speed was adjusted using the ORNL slicer flow calculator to produce comparable bead sizes. For example, using the AT profile at 50 rpm screw speed resulted in a tool traversing speed of 0.06 m/s, while using the MinT profile at 50 rpm screw speed resulted in a tool traversing speed of 0.05 m/s.

Overpressure can reduce the life or damage the lead screw, and so monitoring the extruder pressure is important when printing with new parameters. The BAAM system has a sensor located within the barrel that provides real-time pressure data but is not able to record those measurements. Additionally, the barrel has a 34 MPa pressure relief valve. The pressure is governed by the combination of temperature and feed rate, for example, printing at a low temperature and high feed rate will increase the pressure. Some material manufacturers list the adequate barrel pressure on their data sheets, for ABS 20%wt. carbon fiber the pressure is recommended to be lower than 13.5 MPa. An overpressure inside the barrel can lead to damage of the screw or the barrel itself.

4.1.2 Microscopy and Imaging processing

All specimens were sectioned and mounted to reveal a cross-sectional view normal to the polymer flow direction. Cut specimens were mounted in self-curing resin (Koldmount, MPC Industries, Albany NY US) and subsequently polished using 80-2400 grit papers followed by the use of a 0.05-micron alumina polishing solution. The as-polished specimens were photographed on a Keyence VHX-1000 digital microscope (Keyence Corporation of America, Itasca, IL US) and a Leica MZ16 stereomicroscope (Leica Microsystems Inc., Buffalo Grove, IL US). Imaging analysis to measure the voids was conducted using Vision Assistant 2011 (National Instruments, Austin, TX US) by selecting a region of interest of known area and then extracting the Hue, Saturation, and Luminance (HSL) values (Figure 10-a). The software was calibrated to the scale bar from the microscopic image to determine the pixel-micron conversion factor. A darkness threshold was established to differentiate the voids from the remainder of the materials (Figure 10-b), which resulted in a binary image. A particle analysis built-in function within Vision Assistant determined the area covered by voids (red color) using the binary image. Note that in this manuscript, the volume of voids is not being measured, instead the void percentage is being represented by the area the voids occupy within the bead's cross-section. As a way of gaining confidence in this methodology, already certified copper powder with an average particle size of

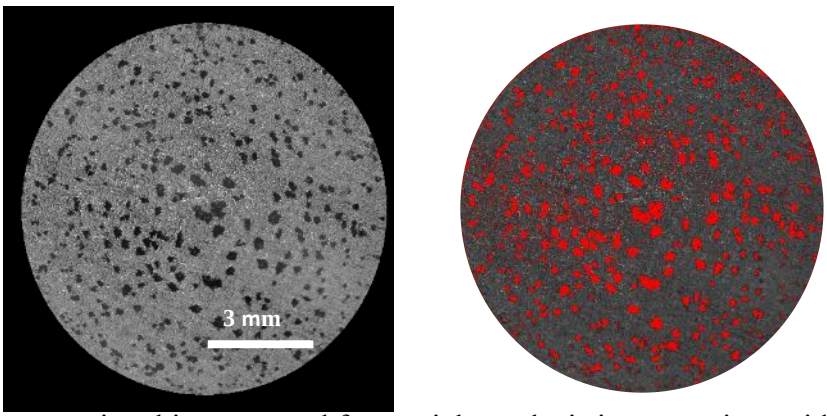

Figure 10: Cross-sectional images used for particle analysis in measuring void size: a) original picture before adding threshold, and b) image after adding threshold to identify voids (red regions).

60 microns was measured with Vision Assistant. The software measured an average particle size of 63 microns, which means the software overestimated the measurement by 5%.

4.1.3 Surface Roughness and Mass Loss Due to Off -Gassing

For each temperature profile and screw speed combination, the time that pelletized material spent within the extrusion tool was measured by depositing a different color material into the barrel while extruding and noting the elapsed time when the material appeared at the exit nozzle. To quantify the mass loss due to off-gassing of volatile organic compounds during the same time period, 2.5 g of pelletized material were wrapped in conventional aluminum foil and placed on a temperature controlled hot plate for the prescribed time. While on the hot plate, the aluminum foil pouch was insulated opposite the side contacting the hot plate. The fiberglass insulation (~50 mm (2 in.) thick with no facing) was used to ensure heat was transferred to the pelletized material within the foil during the short time period. Immediately after heating on the hot plate, each specimen was placed in a desiccator until reaching room temperature after which their mass was collected. The average of five specimens was calculated for each group.

Surface roughness was measured using a SURFTEST SJ-210 surface roughness measuring tester (Mitutoyo America, Aurora, IL US) with a measuring range of 360 micrometers. All samples were composed of at least 3 specimens. For the printed samples, the test was performed on the sides that did not have contact with the tamper or the bed.

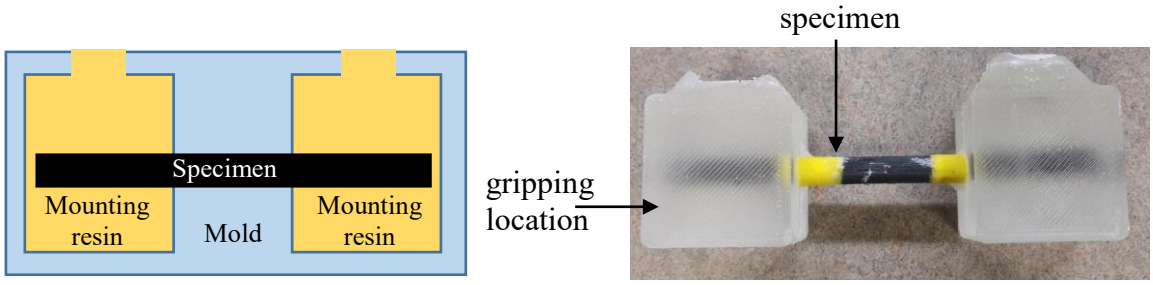

Figure 11: Mold used to mount specimens is shown on the left. On the right, a finished specimen is shown. The grips of the tensile test machine grab the specimen form the gripping location on both sides of the specimen

4.1.4 Tensile test

Tensile tests were performed on 150 rpm samples both printed and extruded for the MinT, AT, and MaxT profile using an adapted version of ASTM D638 standard (ASTM International, 2014). This screw speed was chosen based on the usual printing parameters for this material. The beads were cut to a length of 100 mm and mounted with self-curing resin (Koldmount, MPC Industries, Albany NY) using a mold (Figure 11). The strain-controlled test was performed on an Instron 5800 series (Instron, Norwood, MA) at a strain rate of 5 mm/min. Because of the non-standard shape of the specimen, the strain was not measured and the displacement from the machine was used for all calculations. All samples were composed of at least 3 specimens.

4.2 RESULTS

4.2.1 Analysis of voids

Two types of voids were present in the extruded specimens with distinct regions of occurrence. The first type, being referred to as gas voids was distributed throughout the entire

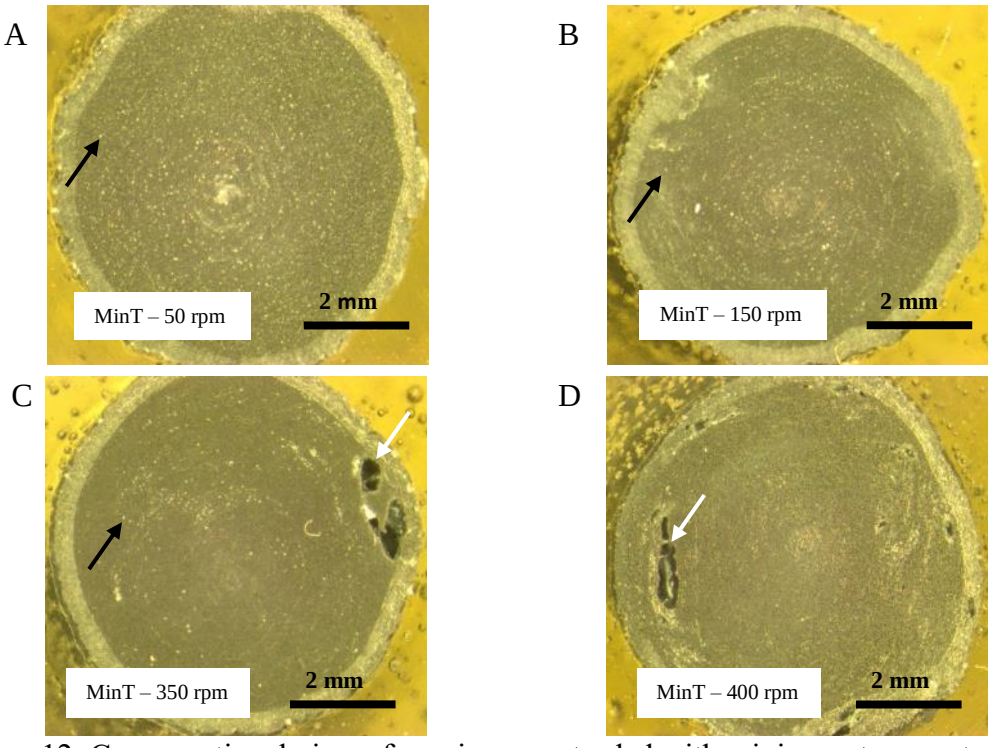

Figure 12: Cross-sectional view of specimens extruded with minimum temperature (MinT) profile: a) 50 rpm, b) 150 rpm, c) 350 rpm, d) 400 rpm. Images taken using stereomicroscopy. Black arrows highlight the gas voids while white arrows point to entrapped air voids

cross-sectioned area. Gas voids are caused, as noted in Arnold et al. (2009), by residual volatiles in the material and/or partial degradation of the material (e.g., release of smaller ABS molecules) during the material's residence in the extruder and the subsequent drop in pressure after exiting the extruder that allows gas expansion. Gas voids were observed in all specimens regardless of the temperature profile and screw speed. Figure 12 shows gas voids (highlighted by black arrows) in the MinT extruded samples for all screw speeds. The second type of voids observed is being referred to as entrapped air voids, which can be seen in Figure 12 as highlighted by white arrows for screw speeds of 350 and 400 RPM. The entrapped air voids were larger and appeared near the periphery of the extrudate, and were caused by air entrapped at the feed throat that did not back-flow from the screw to the hopper due to high screw speeds. This entrapped air was not contained in the individual pellets, but instead came from the 30-70% air by volume that was contained in the feed material (i.e., air between pellets) (Chung 2010). Similar voids, or bubbles, have been observed in single screw extrusion of neat methacrylate-ABS (Park et al. 2017) and natural fiber reinforced thermoplastics where their occurrence increased with temperature and screw speed (Grande and Torres 2004). In other work, the presence of large voids near the periphery of glass-filled polystyrene extrudate was indicative of external surface solidifying that constrained the subsequent core contraction, which ultimately led to void formation (Narkis et al. 1989; Vaxman et al. 1989). Note that at lower screw speeds, the gas voids appeared exclusively, but samples

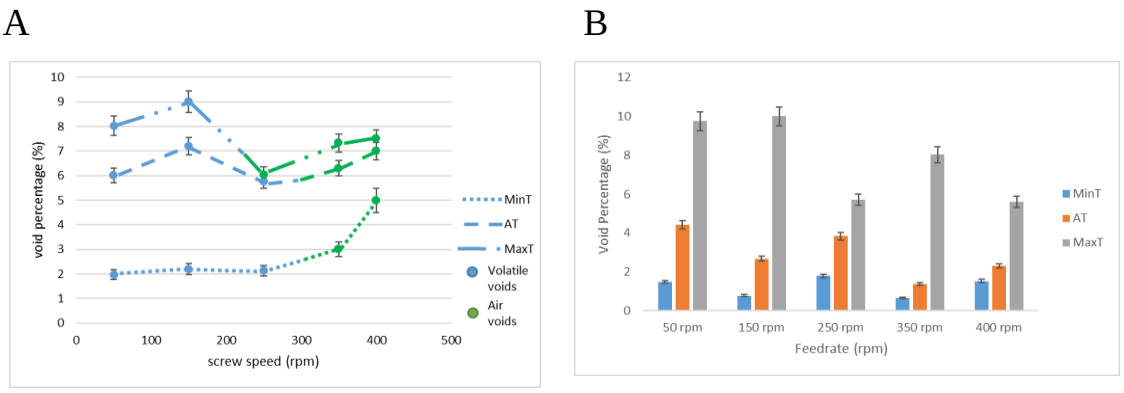

Figure 13: Void percentage of extruded and printed specimens; a) results from extruded specimens, lines are intended to guide the eye and identify the regions where gas and entrapped air voids were observed, b) results from printed specimens.

produced with high screw speeds exhibited both gas and entrapped air voids, as highlighted in Figure 13 and graphically represented in Figure 13 wherein the parameter space explored in this study and its effect on the occurrence of void type is summarized; blue lines represent gas voids and green lines represent entrapped air voids.

Generally, for every screw speed, void percentage increased with the increase of temperature as shown in Figure 13. In other words, for every screw speed void percentage was always lowest at MinT and highest at MaxT. Figure 13 also shows that the spread in void percentage decreased with the increase of screw speed, when considering all temperature profiles. For example, the spread at 50 rpm was 6% voids whereas the spread at 450 rpm was 2.5% voids. This indicates that at high screw speeds, the temperature profile did not strongly impact void percentage. Note that the decrease in spread was not due to the overall decrease in void percentage, but instead the increase in void percentage for the MinT group at high screw speeds.

Recall that the MinT temperature profile maintained all barrel zones below the material's DOT (258°C) and therefore the void percentage was lowest for that group. In fact, the microscopic images and the image analysis of MinT specimens identified an unchanged void percentage until after reaching 250 RPM screw speed (see Figure 12) indicating that the screw speed was not influential at or below 250 rpm. After exceeding 250 rpm in the MinT profile, the presence of entrapped air voids was noted to increase the overall void percentage. Since the AT and MaxT

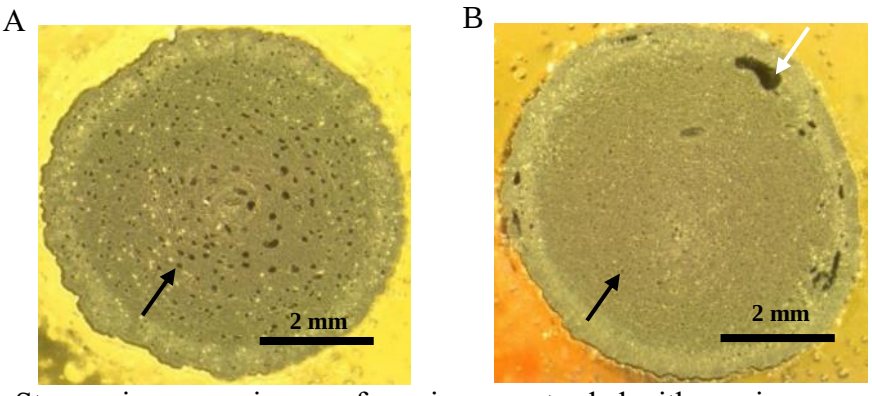

Figure 14: Stereomicroscope image of specimens extruded with maximum temperature (MaxT) profile: a) 50 rpm, b) 400 rpm. Black arrows highlight gas voids while white arrows point to entrapped air voids.

temperature profiles contained barrel zones above the DOT, the material partially decomposed and off-gassed within the extruder, manifesting itself as gas voids in the extrudate since the extruder did not have a vent. In general, for AT and MaxT within the gas void regions of Figure 13, the void content decreased as screw speed increased because the resident time of the material within the extruder decreased (i.e., less off-gassing resulted during the shorter residence time), which has been previously observed in literature (Narkis, et al. 1989). Figure 14 highlights the difference in gas voids where the MaxT – 50 rpm specimen contained larger gas voids in the radius range of 22 to 160 µm. On the other hand, the MaxT – 400 rpm specimen contained smaller gas voids in the radius range of 11 to 20 µm. As with MinT specimens, once the AT and MaxT specimens reached a critical screw speed, the presence of entrapped air voids was observed. For all temperature profiles, entrapped air limits the operating range to lower screw speeds that mitigates its manifestation as entrapped air voids.

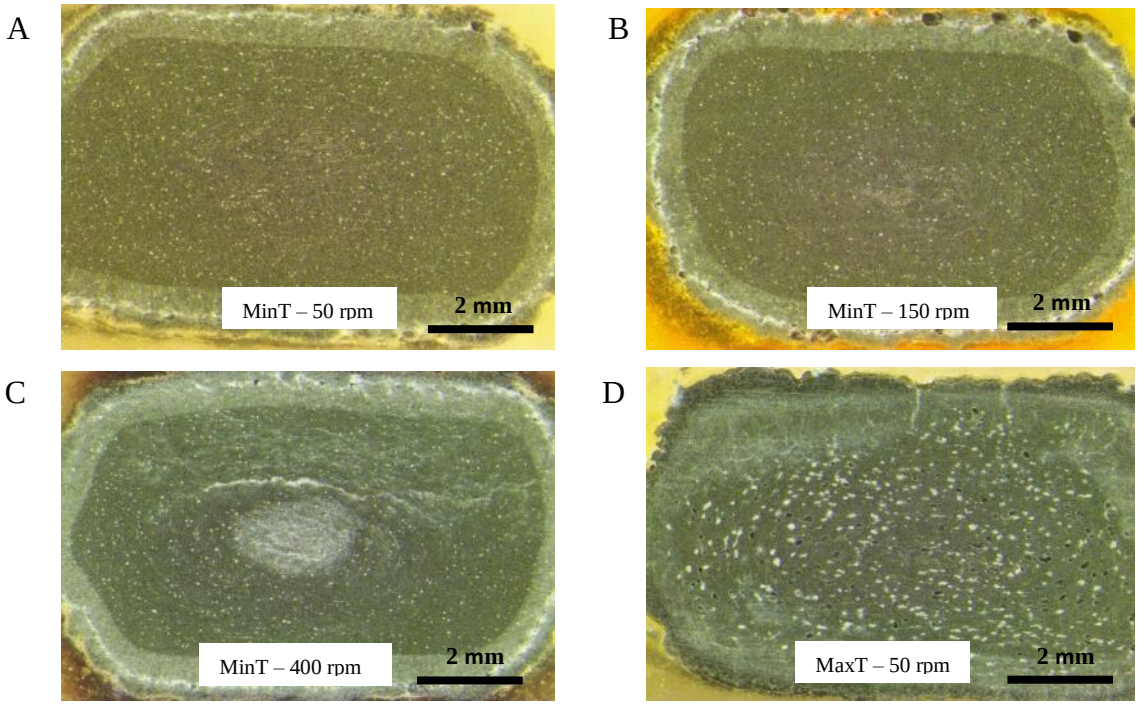

Figure 15: Microscopic view of printed specimens: a) minimum temperature (MinT) profile at 50 rpm screw speed, b) MinT at 150 rpm, c) MinT at 400 rpm, and d) maximum temperature (MaxT) profile at 50 rpm.

Figure 15 shows printed samples at MinT, MaxT and AT in which gas voids are present even after the use of the tamper. However, entrapped air voids were not observed in printed specimens suggesting that the combination of printing conditions (heated print platform, pressure against the platform while extruding, and tampering) allowed the entrapped air to escape the printed bead. Similar to the results from the extruded samples, the MaxT printed samples had the highest void content followed by AT and MinT samples (see Figure 4b). Although the imaging analysis showed that voids were still present in all samples, it is difficult to draw a comparison between extruded and printed samples as the tampering modified the aspect ratio of the voids. That is, the area occupied by a void at any cross section does not capture the potential length change caused by the tamper.

The mass loss due to VOC off-gassing when pellets were heated to 310°C (representative temperature for MaxT) for specific times is reported in Figure 16. Note that 18, 24, 37, and 120 seconds were correlated to residence times associated ith 400, 350, 250, 150, and 50 rpm, respectively. As expected, there was a direct relation between mass loss and time (or inverse relation if the corresponding feed rates are considered) as shown in Figure 15. The inverse relation

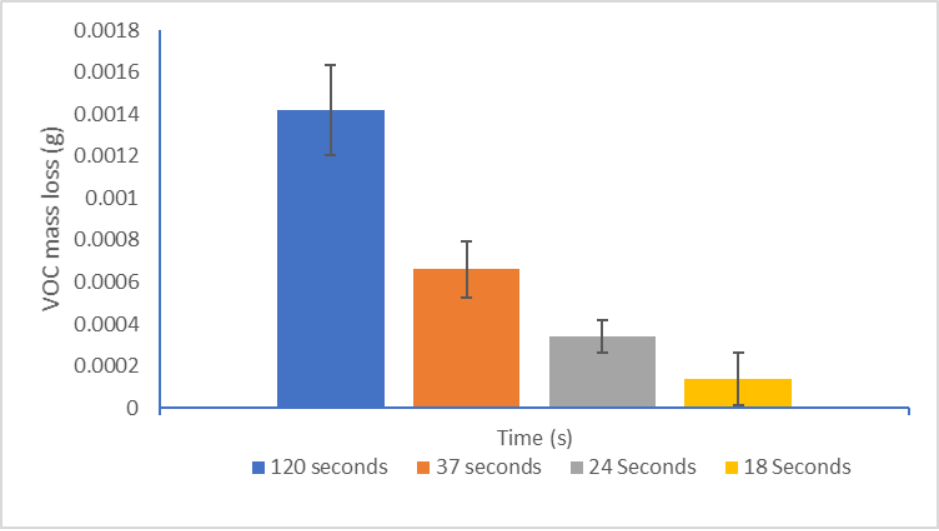

Figure 16: Volatile organic compound mass loss due to off-gassing when using the maximum temperature (MaxT) profile.

shown in Figure 16 corroborates the notion that near or above the DOT, void presence is dominated by VOC off-gassing as mentioned by Narkis, et al.

4.2.2 Surface Roughness

For the extruded MinT and AT samples, the surface roughness showed a clear trend of decreasing surface roughness with increasing screw speed as seen in Figure 8a. Previous literature (Kim and Park 2000) has noted that the surface roughness of glass fiber filled (10 wt %) polystyrene extrudate decreased as the shear rate increased. In the case of the BAAM screw extruder, the screw speed has a direct relation with shear rate at the orifice, and therefore the results observed here are in agreement with that seen in literature. The lower surface roughness measured at high screw speed can be attributed to fiber orientation in the melt flow direction (Kim and Park 2000, Hristov et al. 2006). It was also noted that the shape of the bead transitioned from regular to an irregular shape ("bumpy") as screw speed increased as seen in Figure 17. At 50 rpm, it was possible to see the fibers protruding from the bead while at 400 rpm the bead was smooth and had a glossy appearance. The MaxT samples did not show the same trend, but overall the surface roughness of 350 and 400 rpm specimens was lower than that of the 50 rpm specimens. Surface quality, as measured through surface roughness, has been correlated to water absorption wherein

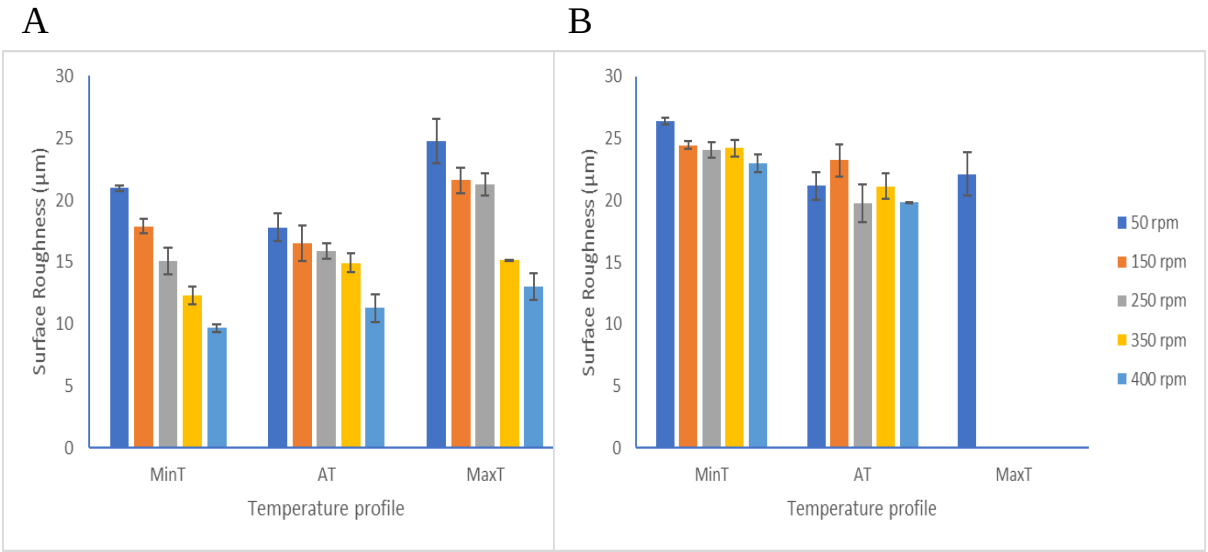

Figure 17: Surface roughness measurements of extruded (A) and printed (B) samples.

the two are directly related (Soury et al. 2011). The characterization performed here suggests that extrudate produced with high screw speeds has higher water resistance when compared to low screw speed extrudate.

Figure 17b also shows the surface roughness of the printed samples was higher when compared to the extruded samples. This was attributed to the effect of the tamper flattening the bead and displacing entrapped air to the surface, causing the protrusion of carbon fibers. The surface roughness of the MaxT– 50 rpm sample was the only result obtained at that temperature profile because the remaining samples had a surface roughness (Ra) over 360 µm, which was not measureable by the instrument being used.

4.3 TENSILE TEST

Tensile tests were performed on samples extruded and printed at 150 rpm using the MinT, AT and MaxT temperature profiles. The general behavior of each extruded sample is represented in Figure 18. The printed specimens had a similar behavior, but due to the action of the tamper the cross-sectional area varied and further measurements are needed to calculate the correct stresses so only extruded specimens results are shown. It should also be noted that for the MinT printed

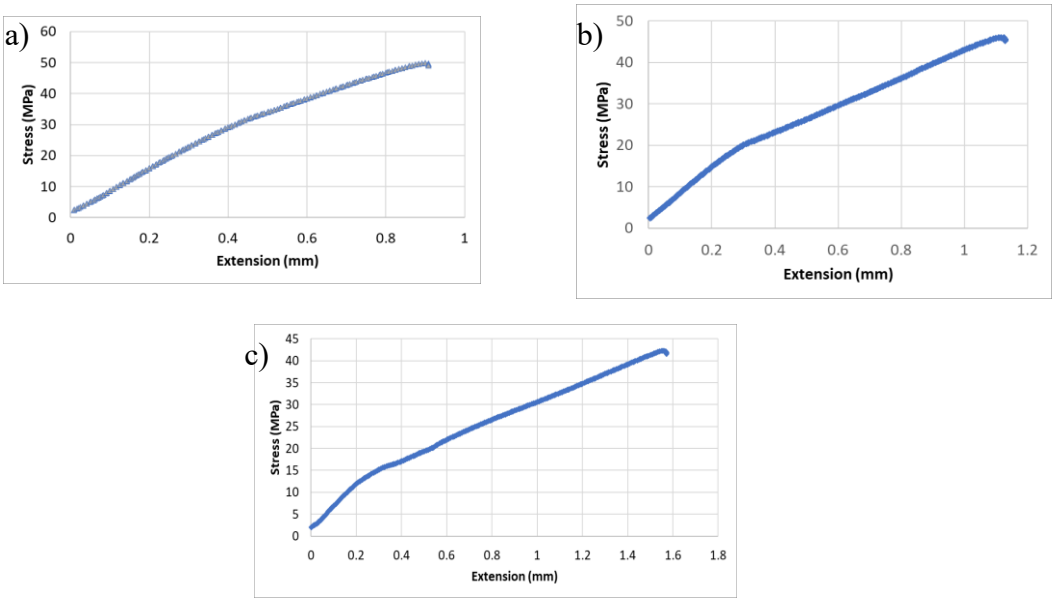

Figure 18: stress – extension graphs of extrudate samples showing the behavior of the material

and extruded samples, only one specimen was broken and the rest were pulled out of the self-curing resin mold. This behavior is attributed to the specimen being stronger (>50 MPa) than the bond between the specimen and the self-curing resin. The high tensile strength is attributed to the low void content seen in the MinT 150 rpm specimen. In the other hand, the AT and MaxT tensile strength was similar which is attributed to the similar void content shown before, with an average ultimate tensile strength of 41 ± 3.77 MPa and 38 ± 3.38 MPa for AT and MaxT respectively. It also noteworthy to mention that the tensile strength values seen for the beads are lower if compared to tensile strength of modified type I specimens of the same material.

4.4 DISCUSSION

For both MinT and AT, extruded and printed samples had voids, with larger voids occurring at higher feed rates. The low temperatures made the material less viscous, which increased the shear effect from the single screw leading to void formation. As stated before, macro-voids around the periphery appeared in extruded samples. This was attributed to the difference between the cooling rate of the external and internal parts of the bead caused by the high feed rates.

Even though the tamper reduced the majority of macro-voids in printed samples, voids were still present. The surface roughness increased between extruded samples to printed samples in almost all settings. This is due to the displacement of fibers by entrapped air traveling within the bead caused by the tamper's action. It was also noted that the pressure inside the barrel was higher than the manufacturer's recommended value for high feed rates at both MinT and AT.

For MaxT, image analysis showed a substantial void content at low feed rates. This is a result of the off-gassing of VOC's, which was confirmed by the experimental setup presented in this paper. At 350 and 400 rpm, the macro-voids are created similarly to the MinT and AT samples. Even with the action of the tamper, the printed beads showed a high void content. The pressure inside the barrel did not exceed recommended levels at any point. Additionally, at MaxT the material started decomposing after spending time inside the barrel. Overall, the UTS of the beads was affected by the increase of void content especially between MinT and AT.

Chapter 5: Tensile behavior

5.1 Materials and methods

5.1.1 Specimen fabrication

The material chosen for this work was Electrafil J-1200 CF20 3DP (Techmer PM, Clinton, Tennessee, US) which is ABS20%wt. carbon fiber. The material was dried in accordance to manufacturer recommendations for 4 hr. at 80 °C. A rectangular part was printed using a Cincinnati BAAM-100 (Cincinnati Inc. Harrison, OH US) using a 7.62 mm (0.3 in) nozzle coupled with a tampering system. The square part measured to be 165.1 cm (65 in) X 177.8 cm (70 in), 12 cm tall and 25.91 mm thick (1.02 in). The bead width for this part was set to 8.64 mm (0.34 in) and the layer height was 3.81 mm (0.15 in). The dimensions of the part were chosen to allow for 3 modified type I specimens (Duty, *et al*. 2017) to be harvest from every side with the longest side of the specimen being the same direction as the toolpath direction. The specimens are similar to the ones used by Duty *et al* pictured in Figure 19, with the difference in the length of the gripping section. The dimensions had to be modified due to a constraint with the machining process.

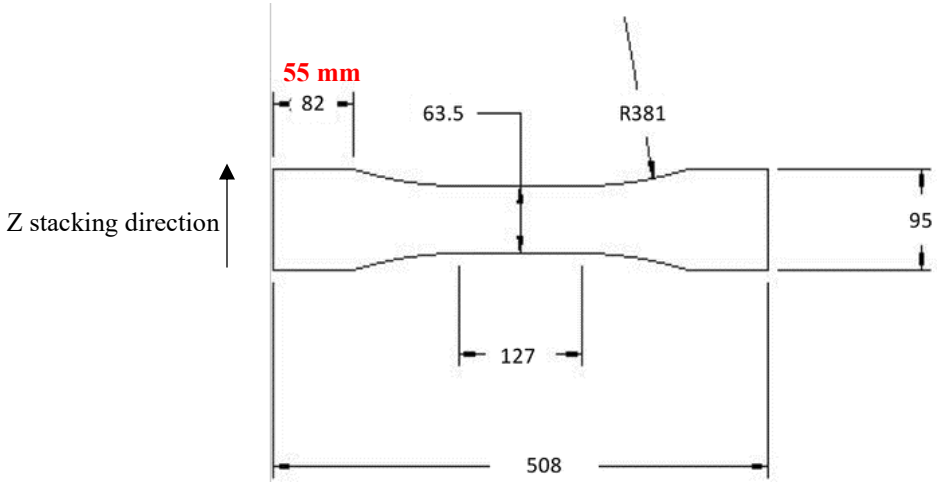

Figure 19: The specimens used for this work are the same modified type I specimens used by Duty *et al* (2015) with the only difference being a shorter gripping section of 50 mm.

Table 5: Printing parameters

			Heater (°C)				Printing speed
Melt	1	2	3	4	5	6	114.3 mm/s
270	246	260	270	265	270	266	4.5 in/s

Table 5 shows the BAAM-specific settings used to fabricate the specimens. To ensure adequate bonding between layers of the material, the 1-D heat transfer model developed by Compton *et al* (2017) was implemented (Appendix A). The only inputs of the model that were modified were the layer time and deposition temperature. The layer time was calculated from the G-code and the chosen printing speed of 114.3 mm/s (4.5 in/s). The layer time was calculated to be 180 seconds, the value was then inputted into the model with a deposition temperature of 165 °C. As seen in Figure 20, all layers after layer 4 remained over the T_g (~105°C) thus assuring a good bond between layers. If a lower deposition temperature was chosen, the layer would have

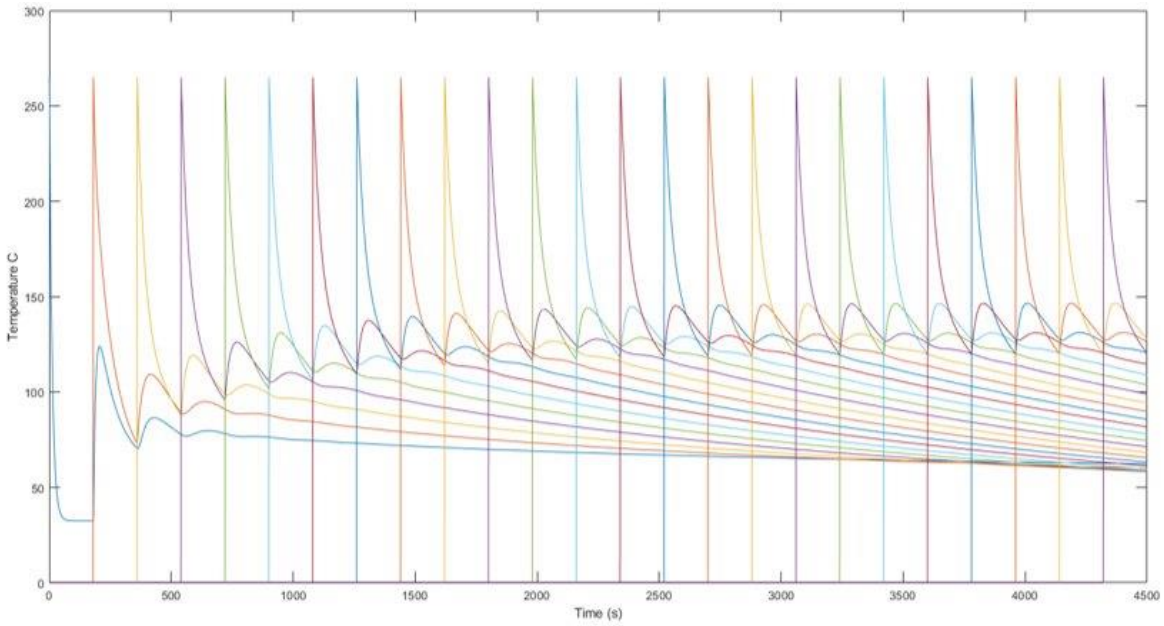

Figure 20: Temperature vs Time graph from the Compton *et al* heat transfer model

cool down below the desired threshold. The height of the rectangular part was chosen to allow for the first 4 layers to be discarded during manufacturing of the specimen.

The printed rectangle was sectioned with a manual saw and each individual piece was machined to the required dimension. The machining process was conducted by securing the part using custom soft grips and machining 3 sides of the specimen. Then, the part was removed, flipped and secured to face the last side of the specimen. To avoid problems with cracking and surface quality, the specimens were machined using a diamond coated end mill. The as-machined specimens were placed in an incubator at 23 °C and 50% humidity for at least 88 hours in accordance with ASTM D618 (ASTM International, 2013). Duty *et al* (2017) and Schnittker *et al* (2018) used procedure B from the ASTM D618 which entails placing the specimen at 50 °C for 48 hr. and then placing them in a desiccator for another 15 hr. As noted in the standard, this procedure is used more often with thermosets or when the moderate effects of moderate drying are to be determined.

5.1.2 Tensile testing

Specimens were tested using an MTS landmark 370 servo-hydraulic system (MTS, Eden Prairie, MN US) equipped with a 100 kN load cell following ASTM D638. To produce results

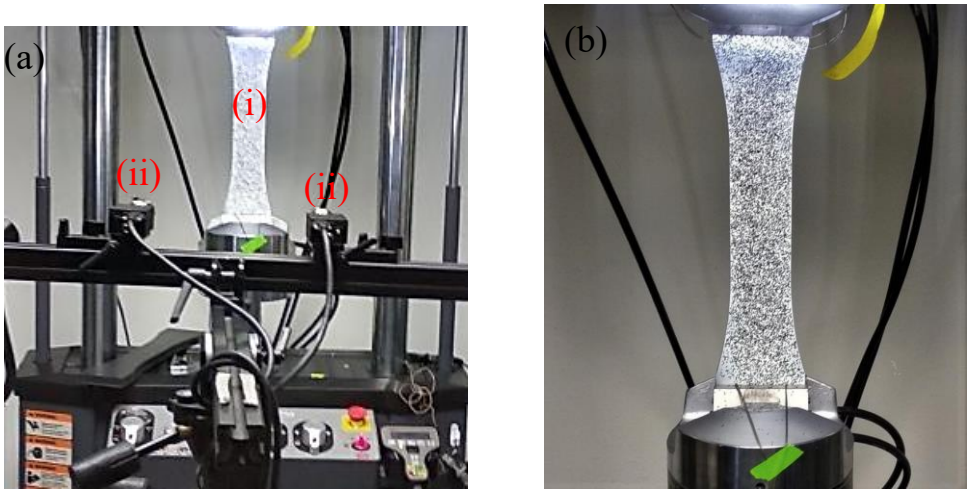

Figure 21: a) Digital image correlation (DIC) set-up showing (i) specimen and (ii) cameras. b) picture of the specimen with the pattern needed for DIC

comparable to Duty *et al* (2017), the strain rate was chosen to be 0.025 mm/s. A digital correlation system (Correlated Solutions, Irmo, SC US) was used to capture strain measurements (Figure 21). To capture DIC images, the specimen had to be prepared by applying a pattern full of speckles, by tracking the speckles as the specimen deforms the DIC can capture strain measurements. First, a flat-white base coat was uniformly applied, immediately after, 1 mm crafting glitter was randomly applied on the gauge length. Finally, a layer of clear coating was applied to reduce the shinning effect caused by the glitter. This procedure was successfully used by Schnittker *et al* (2018), showing acceptable speckle patterns which resulted in consistent correlation of images. For strain measurements, the DIC system was calibrated following manufacturer recommendations, and the data was recorded at 1 s intervals.

5.2 RESULTS

5.2.1 Tensile test

The DIC data was used to calculate the elastic modulus, yield strength and ultimate tensile strength (UTS). Table 6 shows the experimental tensile test results compared to the ones obtained by Duty et al (2017). It should be noted that the screw and barrel used by Duty et al differs from the one used in this work. The average ultimate tensile strength was calculated to be 62.98 ± 2.16 MPa which is well within the range of results that Duty et *al* obtained. For this present work, the printing parameters were optimized to achieve a consistent layer temperature well over T_g during printing of the specimens. In previous work (Schnittker, *et al.* 2019), ABS20%wt glass fiber specimens were built using the same parameters used by Duty *et al* but the results demonstrated a

Table 6: Mechanical properties of ABS 20%wt carbon fiber compared against Duty *et al* (2017)

Property	Tensile test results					Duty, *et al*. (2017)
	Sample 1	Sample 2	Sample 3	Sample 4	Sample 5	
Ultimate tensile strength (MPa)	60.47	66.11	62.11	62.15	64.06	~51 - 66
Elastic Modulus (GPa)	12.88	12.43	12.49	12.06	13.00	~6 – 12
Yield Strength (MPa)	45	43	45	40	40	n/a

decrease in tensile strength. This demonstrates that differences within the extruder (i.e. screw, barrel, heaters) affects the processing parameters needed to achieve good bonding between layers. Overall, the results showed consistency among the specimens with a coefficient of variation of 0.03 for the tensile strength. This emphasizes that the bond between layers was strong and consistent all throughout the rectangle part. When building at large-scale, sometimes consistency can be affected due to the long layer time.

The stress-strain curves for the ABS20%wt. carbon fiber material are plotted in Figure 22. From the plot, the yield cannot be easily measured. The yield strength was calculated by adding each point of the stress-strain curve into a linear fit until the confidence level went under 99.5% (R^2<0.995). The average yield strength for the sample was 42.6 ± 2.5 MPa. The yield strength is vital for cyclic testing as the selected stress levels must fall within the linear region to avoid hysteresis from plastic deformation. The graph also demonstrates how similar the curves are from one another, just adding the low coefficient of variance.

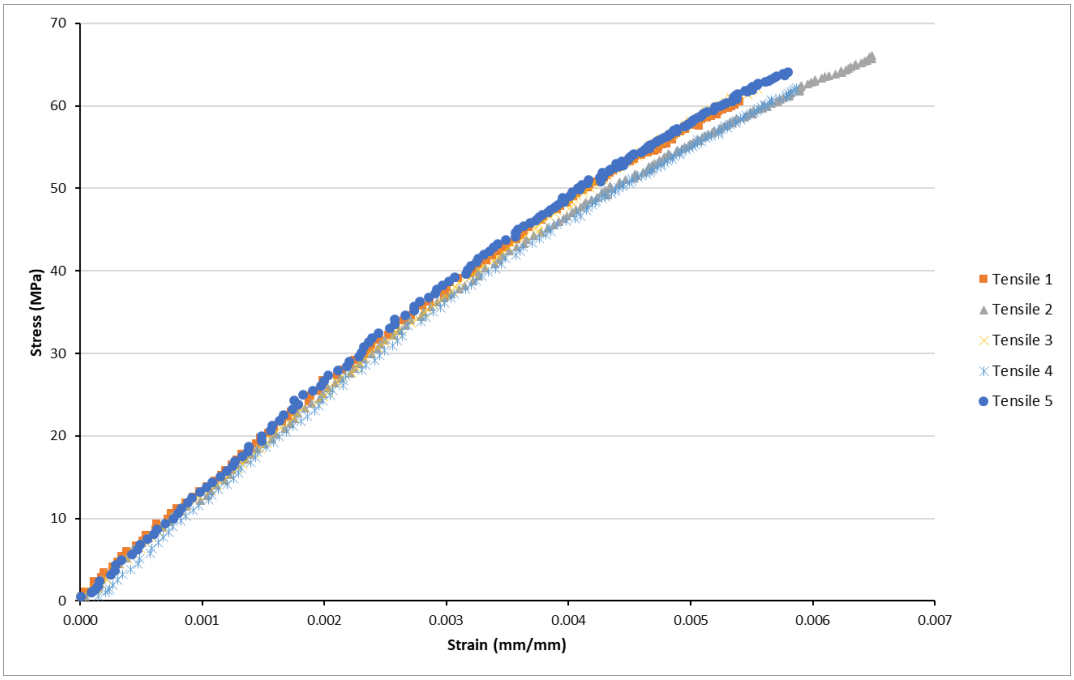

Figure 22: Stress-strain curve for ABS20%wt. carbon fiber

Chapter 6: Conclusion and recommendation

6.1 Conclusion

This paper presents a study on the effect that feed rate and temperature have on the presence of voids within beads extruded and printed using ABS 20%wt. carbon fiber on the Big Area Additive Manufacturing machine. Temperature recommendations from the material manufacturer were used to create a maximum (MaxT), average (AT), and minimum (MinT) temperature profiles. Using these profiles, extruded (no tamper) and printed (with tamper) samples were created for different feed rates (50, 150, 250, 350, and 400 rpm). Gas voids were found to appear in all samples scattered across the entire radius of the specimen. Those gas voids are created by the volatile off gassing and decomposition of the material. Larger entrapped air voids were found in samples of 250 rpm or higher on the periphery of the specimens. Those voids are caused by the introduction of air into the barrel of the extruder due to the fast material intake. It was also discovered that even when printing at low temperatures, micro-voids are present within a bead and the tamper does not eliminate all voids. A method to perform tensile test on extruded and printed single beads was developed. A mold was used to mount the specimens into two blocks of self-curing resin. Tensile tests showed that void content affects the tensile strength of a single bead but the effect on printed samples is yet to be determined. The MinT profile is belived to have the highest strength as only one specimen failed and the rest pulled out of the resin mount. When creating simulations of this process, internal voids should be added into the model to obtain more accurate results.

Tensile tests of the modified type I specimens showed comparable results to other published work. The young's modulus was calculated to be ~13 GPa which is higher than the published data from Duty *et al*. (2017) for the same material. The difference is believed to occur because the extrusion temperature used in this paper was 40 degrees (160 °C) higher than the one used by Duty. In the same paper (Duty *et al.* 2017), similar modulus values were found for ABS 15%wt. carbon fiber extruded at 160 °C.

A non-standard CNC tool was mounted into the BAAM system at UTEP through modification of the firmware, controls and hardware of the system. In partnership with Cincinnati

Inc, a process sequence was developed and then mapped into G-code and M-code. Autodesk developed a CAM post specifically to the tool to directly obtain the inverse kinematics and M-code needed for wire embedding operations. The tool was successfully tested by Cincinnati and UTEP.

6.2 RECOMMENDATION FOR FUTURE WORK

Further work should include an understanding of the effect of over and under drying on material properties because of the variability this can introduce in the material affecting mechanical properties such as yield strength. Additionally, further investigation on the effect that each heater has on the void content of the material is needed. Also, future work should include understanding the effect that extrusion temperature and layer temperature have on the bond strength of layer in the Z direction (stacked direction). Using the static tensile test information gathered in this paper, fatigue tests should be performed to fully understand the mechanical behavior of this material.

References

[Afrose, M. F., Masood, S. H., Iovenitti, P., Nikzad, M., & Sbarski, I. (2016). Effects of part build orientations on fatigue behaviour of FDM-processed PLA material. Progress in Additive Manufacturing, 1(1-2), 21-28.]

[Agarwal, K., Kuchipudi, S. K., Girard, B., & Houser, M. (2018). Mechanical properties of fiber reinforced polymer composites: A comparative study of conventional and additive manufacturing methods. Journal of Composite Materials, 52(23), 3173-3181.]

[Ajinjeru, C., Kishore, V., Chen, X., Lindahl, J., Sudbury, Z., Arabi, A., ... & Duty, C. E. (2016). The Influence of Rheology on Melt Processing Conditions of Amorphous Thermoplastics for Big Area Additive Manufacturing (BAAM). In 27th Annual International Solid Freeform Fabrication Symposium, Austin, TX (pp. 754-762).]

[Ajinjeru, C., Kishore, V., Sudbury, T. Z., Lindahl, J., Hassen, A., Post, B., ... & Duty, C. (2017). The Influence of Rheology on Melt Processing Conditions of Carbon Fiber Reinforced Polyetherimide for Big Area Additive Manufacturing (BAAM).]

[Alex Roschli, Katherine T. Gaul, Alex M. Boulger, Brian K. Post, Phillip C. Chesser, Lonnie J. Love, Fletcher Blue, Michael Borish, Designing for Big Area Additive Manufacturing, Additive Manufacturing, Volume 25, 2019, Pages 275-285, ISSN 2214-8604, https://doi.org/10.1016/j.addma.2018.11.006.]

[Ambriz, S. D. (2015). *Design and development of the portable build platform and heated travel envelope for the Multi 3D manufacturing system*. The University of Texas at El Paso.]

[Arnold, J. C., Alston, S., & Holder, A. (2009). Void formation due to gas evolution during the recycling of Acrylonitrile–Butadiene–Styrene copolymer (ABS) from waste electrical and electronic equipment (WEEE). Polymer Degradation and Stability, 94(4), 693-700.]

[Arrieta, E., Haque, M. S., Mireles, J., Stewart, C. M., Carrasco, C., & Wicker, R. (2018). Mechanical behavior of differently oriented EBM Ti-6Al-4V components using digital image correlation. J. Eng. Mater. Technol.]

[ASTM International. (2013). ASTM D618-13 Standard Practice for Conditioning Plastics for Testing. Retrieved from https://doi.org/10.1520/D0618-13]

[ASTM International. (2014). *ASTM E1131-08(2014) Standard Test Method for Compositional Analysis by Thermogravimetry*. Retrieved from https://doi.org/10.1520/E1131-08R14]

[ASTM International. (2014). *ASTM E1356-08(2014) Standard Test Method for Assignment of the Glass Transition Temperatures by Differential Scanning Calorimetry*. Retrieved from https://doi.org/10.1520/E1356-08R14]

[ASTM International. (2015). *ASTM D4440-15 Standard Test Method for Plastics: Dynamic Mechanical Properties Melt Rheology*. Retrieved from https://doi.org/10.1520/D4440-15]

[ASTM International. (2017). *ASTM E2008-17 Standard Test Methods for Volatility Rate by Thermogravimetry*. Retrieved from https://doi.org/10.1520/E2008-17]

[ASTM International. (2017). ASTM E2550-17 Standard Test Method for Thermal Stability by Thermogravimetry. Retrieved from https://doi.org/10.1520/E2550-17]

[ASTM International. (2018). *ASTM E473-18 Standard Terminology Relating to Thermal Analysis and Rheology*. Retrieved from https://doi.org/10.1520/E0473-18]

[ASTM International. (2018). *ASTM E794-06(2018) Standard Test Method for Melting And Crystallization Temperatures By Thermal Analysis*. Retrieved from https://doi.org/10.1520/E0794-06R18]

[ASTM International. (2018). ASTM ISO/ASTM52910-18 Additive manufacturing — Design — Requirements, guidelines and recommendations. Retrieved from https://doi.org/10.1520/F3154-18]

[Boldizar, A., Möller, K., 2003. Degradation of ABS during repeated processing and accelerated ageing. Polymer Degradation and Stability 81, 359–366. https://doi.org/10.1016/S0141-3910(03)00107-1]

[Brenken, B., Barocio, E., Favaloro, A., Kunc, V., & Pipes, R. B. (2019). Development and validation of extrusion deposition additive manufacturing process simulations. Additive Manufacturing, 25, 218-226.]

[C.W. Ziemian, R.D. Ziemian, K.V. Haile, Characterization of stiffness degradation caused by fatigue damage of additive manufactured parts, Materials & Design, Volume 109, 2016, Pages 209-218, ISSN 0264-1275, https://doi.org/10.1016/j.matdes.2016.07.080.]

[Chung, C., 2010. Extrusion of Polymers 2E: Theory and Practice, 2 edition. ed. Hanser, Munich : Cincinnati.]

[Cincinnati Incorporated, BAAM - Big Area Additive Manufacturing. (n.d.). Retrieved December 3, 2018, from https://www.e-ci.com/baam/]

[Compton, B. G., Post, B. K., Duty, C. E., Love, L., & Kunc, V. (2017). Thermal analysis of additive manufacturing of large-scale thermoplastic polymer composites. Additive Manufacturing, 17, 77-86.]

[Coronel Jr, J. L. (2015). *Multi 3D system: Advanced manufacturing through the implementation of material handling robotics*. The University of Texas at El Paso.]

[Crump, S. (1992). US Patent No. 5121329A.]

[Degrieck, J., & Van Paepegem, W. (2001). Fatigue damage modeling of fibre-reinforced composite materials. *Applied mechanics reviews*, *54*(4), 279-300.]

[Duty, C. E., Kunc, V., Compton, B., Post, B., Erdman, D., Smith, R., ... & Love, L. (2017). Structure and mechanical behavior of Big Area Additive Manufacturing (BAAM) materials. Rapid Prototyping Journal, 23(1), 181-189.]

[Espalin, D., Muse, D. W., MacDonald, E., & Wicker, R. B. (2014). *3D Printing multifunctionality: structures with electronics*. The International Journal of Advanced Manufacturing Technology, 72(5-8), 963-978.]

[Espalin, David, *"High Feed Rate Wire Heating and Embedding for Large Area Additive Manufacturing of Parts Containing Embedded Electronic Functionality"* (2017). ETD Collection for University of Texas, El Paso. AAI10825126. https://digitalcommons.utep.edu/dissertations/AAI10825126]

[Forrest, J. A., Dalnoki-Veress, K., Stevens, J. R., & Dutcher, J. R. (1996). Effect of free surfaces on the glass transition temperature of thin polymer films. Physical review letters, 77(10), 2002.]

[Francis, V., & Jain, P. K. (2016). Experimental investigations on fused deposition modelling of polymer-layered silicate nanocomposite. Virtual and Physical Prototyping, 11(2), 109-121.]

[GE Reports. (2017, June). Retrieved from https://www.ge.com/reports/ge-building-worlds-largest-additive-machine-3d-printing-metals/]

[Goh, G. D., Dikshit, V., Nagalingam, A. P., Goh, G. L., Agarwala, S., Sing, S. L., ... & Yeong, W. Y. (2018). Characterization of mechanical properties and fracture mode of additively manufactured carbon fiber and glass fiber reinforced thermoplastics. *Materials & Design*, *137*, 79-89.]

[Grande, C., Torres, F.G., 2005. Investigation of fiber organization and damage during single screw extrusion of natural fiber reinforced thermoplastics. Advances in Polymer Technology 24, 145–156. https://doi.org/10.1002/adv.20037]

[Grimm, T. (2004). User's guide to rapid prototyping. Society of Manufacturing Engineers.]

[Hild, F., & Roux, S. (2006). Digital image correlation: from displacement measurement to identification of elastic properties–a review. *Strain*, *42*(2), 69-80.]

[Hill, C., Rowe, K., Bedsole, R., Earle, J., & Kunc, V. (2016, May). Materials and process development for direct digital manufacturing of vehicles. In SAMPE Long Beach 2016 Conference and Exhibition.]

[Hristov, V., Takács, E., Vlachopoulos, J., 2006. Surface tearing and wall slip phenomena in extrusion of highly filled HDPE/wood flour composites. Polymer Engineering & Science 46, 1204–1214. https://doi.org/10.1002/pen.20592]

[Huang, B., & Singamneni, S. (2015). Raster angle mechanics in fused deposition modelling. Journal of Composite Materials, 49(3), 363-383.]

[Hull, C. (1986). US Patent No. 4575330A.]

[ISO/ASTM52900-15, A. (2015). Standard Terminology for Additive Manufacturing – General Principles. West Conshohocken, PA: ASTM International.]

[John Lee, Adam Huang, (2013) "Fatigue analysis of FDM materials", Rapid Prototyping Journal, Vol. 19 Issue: 4, pp.291-299, https://doi.org/10.1108/13552541311323290]

[Kamesh Tata, Georges Fadel, Amit Bagchi, Nadim Aziz, (1998) "Efficient slicing for layered manufacturing", Rapid Prototyping Journal, Vol. 4 Issue: 4, pp.151-167, https://doi.org/10.1108/13552549810239003]

[Karahaliou, E.-K., Tarantili, P.A., 2009. Stability of ABS compounds subjected to repeated cycles of extrusion processing. Polymer Engineering & Science 49, 2269–2275. https://doi.org/10.1002/pen.21480]

[Kim, J.K., Park, S.H., 2000. Fiber orientation and rheological properties of short fiber-reinforced plastics at higher shear rates. Journal of Materials Science 35, 1069–1078. https://doi.org/10.1023/A:1004782924666]

[Liang, M., Shemelya, C., MacDonald, E., Wicker, R., & Xin, H. (2015*). 3-D printed microwave patch antenna via fused deposition method and ultrasonic wire mesh embedding technique*. IEEE Antennas and Wireless Propagation Letters, 14, 1346-1349.]

[Lopes, A. J., Lee, I. H., MacDonald, E., Quintana, R., & Wicker, R. (2014). *Laser curing of silver-based conductive inks for in situ 3D structural electronics fabrication in stereolithography*. Journal of Materials Processing Technology, 214(9), 1935-1945.]

[Love, L. J., Kunc, V., Rios, O., Duty, C. E., Elliott, A. M., Post, B. K., ... & Blue, C. A. (2014). The importance of carbon fiber to polymer additive manufacturing. Journal of Materials Research, 29(17), 1893-1898.]

[Love, L., Post, B., & Roschli, A. (2017). Wide and High Additive Manufacturing (WHAM). CRADA FINAL REPORT NFE-16-06111.]

[Macdonald, E., Salas, R., Espalin, D., Perez, M., Aguilera, E., Muse, D., & Wicker, R. B. (2014). 3D printing for the rapid prototyping of structural electronics. *IEEE access*, *2*, 234-242.]

[Mandell, J. F., Huang, D. D., & McGarry, F. J. (1981). Fatigue of glass and carbon fiber reinforced engineering thermoplastics. Polymer Composites, 2(3), 137-144.]

[Mason, J. J., Rosakis, A. J., & Ravichandran, G. (1994). On the strain and strain rate dependence of the fraction of plastic work converted to heat: an experimental study using high speed infrared detectors and the Kolsky bar. Mechanics of Materials, 17(2-3), 135-145.]

[Mezger, T. G. (2006). The rheology handbook: for users of rotational and oscillatory rheometers. Vincentz Network GmbH & Co KG.]

[Murphy, M., (2019). You can now 3D-print a house in under a day. Retrieved from https://qz.com/1227301/sxsw-2018-affordable-3d-printed-houses-from-icon-and-charity-new-story-debuted-in-austin/]

[Myers, W; Tennant, A. 1949. US patent office US2567960A]

[N. Turner, B., Strong, R., & A. Gold, S. (2014). A review of melt extrusion additive manufacturing processes: I. Process design and modeling. Rapid Prototyping Journal, 20(3), 192-204.]

[Narkis, M., Vaxman, A., Kenig, S., & Siegman, A. (1989). Quantitative measurement of fiber orientation and fracture, void and weld-lines in short fiber reinforced thermoplastic composites. Thermoplastic composite materials, 307-318.]

[Nouri, H., Meraghni, F., & Lory, P. (2009). Fatigue damage model for injection-molded short glass fibre reinforced thermoplastics. *International Journal of Fatigue*, *31*(5), 934-942.]

[Park, H., Kim, B., Gim, J., Han, E., Rhee, B., 2017. A Study on the Entrapped Air Bubble in the Plasticizing Process. Proceedings from the 2017 Society of Plastics Engineers Annual Technical Conference.]

[Rauwendaal, C. (2019). *Understanding extrusion*. Cincinnati, OH: Hanser Publications. doi: https://doi.org/10.3139/9781569906996.fm.]

[Rittel, D. (2000). An investigation of the heat generated during cyclic loading of two glassy polymers. Part I: Experimental. Mechanics of Materials, 32(3), 131-147.]

[Rundle, G. (2014). A Revolution in the Making. Affirm Press.]

[Sandia National Lab. (2018, April). Retrieved from https://share-ng.sandia.gov/news/resources/news_releases/consortium_awards/#.WvOATIgvyM8]

[Saunders, S. (2018). 3DPrint.com. Retrieved from https://3dprint.com/209940/navair-1000-3d-printed-parts-2018/]

[Schawe, J. E. K. (1995). Principles for the interpretation of modulated temperature DSC measurements. Part 1. Glass transition. Thermochimica Acta, 261, 183-194.]

[Schnittker, K., Arrietaa, E., Jimenez, X., Espalin, D., Wicker, R., Roberson, D. (2019) Integrating digital image correlation in mechanical testing for the materials characterization of big area additive manufacturing feedstock. Additive manufacturing Journal]

[Shemelya, C. M., Zemba, M., Liang, M., Espalin, D., Kief, C., Xin, H., ... & MacDonald, E. W. (2015, May). *3D printing multi-functionality: Embedded RF antennas and components*. In 2015 9th European Conference on Antennas and Propagation (EuCAP) (pp. 1-5). IEEE.]

[Shenoy A.V. (1999) Basic rheological concepts. In: Rheology of Filled Polymer Systems. Springer, Dordrecht]

[Sophia Ziemian, Maryvivian Okwara, Constance Wilkens Ziemian, (2015) "Tensile and fatigue behavior of layered acrylonitrile butadiene styrene", Rapid Prototyping Journal, Vol. 21 Issue: 3, pp.270-278, https://doi.org/10.1108/RPJ-09-2013-0086]

[Soury, E., Behravesh, A., Jam, N.J., Haghtalab, A., 2013. An experimental investigation on surface quality and water absorption of extruded wood–plastic composite. Journal of Thermoplastic Composite Materials 26, 680–698. https://doi.org/10.1177/0892705711428656]

[Tiganis, B.E., Burn, L.S., Davis, P., Hill, A.J., 2002. Thermal degradation of acrylonitrile–butadiene–styrene (ABS) blends. Polymer Degradation and Stability 76, 425–434. https://doi.org/10.1016/S0141-3910(02)00045-9]

[WHAM, there's a new "largest 3D printer in the world" in town. (2018). 3D printing media network. Retrieved from https://www.3dprintingmedia.network/wham-theres-a-new-largest-composite-3d-printer-in-the-world-in-town/]

[Zhong, W., Li, F., Zhang, Z., Song, L., & Li, Z. (2001). Short fiber reinforced composites for fused deposition modeling. *Materials Science and Engineering: A*, *301*(2), 125-130.]

Glossary

AM: Additive Manufacturing

DIY: Do-it-yourself

HMI: Human machine interaction

ODT: Decomposition onset temperature

Appendix A

```
% 1-D Heat Transfer Model for BAAM
% Based on work by ORNL
% Xavier Jimenez 2018
clc
clear
% Define Material Properties

k    = 0.17; % Thermal Conductivity [W/m*K]
c_p = 1640; % Specific heat capacity [J/Kg*K]
T_g = 110;  % Glass transition temperature [degrees C]
p    = 1140; % Density [Kg/m^3]
e    = 0.87; % Emissivity
h    = 8.5;  % Natural convection coefficient [W/m^2*K]
delta = 0.0000000567; % Boltzman's constant

% Define printing parameters
T_dep = 260;    % Deposition temperature [degrees C]
T_bed = 65;     % Bed temperature [degrees C]
T_amb = 18;     % Ambient temperature [degrees C]
d     = 4.064; % Layer height [mm]
L     = 0.358; % Wall height [m]
w     = 0.02;  % Wall thickness [m]
dx    = 0.00254;  % Nodal spacing [m]



T = zeros (25,40,25); % preallocation for speed
ii = 0;
for j = 1:1:25
    T(j,1,j) = T_dep; %New layer at T_dep is added every iteration
    jj = 0;
for dt = 1:1:408 % time steps from 1 to 10 layers time, with a layer
 time of 39 s
    ii = 1 + ii;
    jj = jj + 1;
for i = 1:1:j


h_rad = e*delta*(T(i,dt,j) + T_amb)*(T(i,dt,j)^2 + T_amb^2);
    if i == 1 && j ~= 1
        %bottom node
        T(i,dt+1,j) = ((((2*k*w)/dx)*(T_bed - T(i,dt,j)) + ((2*k*w)/
dx)*(T(i+1,dt,j) - T(i,dt,j)) + dx*(h + h_rad)*(T_amb - T(i,dt,j)))/
((p*c_p*w*dx)/(2*0.77))) + T(i,dt,j);


    elseif i == 1 && j == 1
        %first layer
        T(i,dt+1,j) = ((((k*w)/dx)*(T_bed - T(i,dt,j)) + (dx*(h +
 h_rad)*(T_amb - T(i,dt,j))) + w*(h + h_rad)*(T_amb - T(i,dt,j)))/
((p*c_p*w*dx)/(2*0.77))) + T(i,dt,j);
```

```
    elseif i == j
        %top formula
         T(i,dt+1,j) = ((((k*w)/dx)*(T(i-1,dt,j) - T(i,dt,j)) + (dx*(h
 + h_rad)*(T_amb - T(i,dt,j))) + w*(h + h_rad)*(T_amb - T(i,dt,j))))/
((p*c_p*w*dx)/(2*0.77))) + T(i,dt,j);



    else
        %middle formula
         T(i,dt+1,j) = ((((k*w)/dx)*(T(i-1,dt,j) - T(i,dt,j)) +
 ((k*w)/dx)*(T(i+1,dt,j) - T(i,dt,j)) + 2*dx*(h + h_rad)*(T_amb -
 T(i,dt,j)))/((p*c_p*w*dx)/(0.77))) + T(i,dt,j);



    end

 for ww = 1:25 % This for loop is use to transfer the T values from 3D
 array to 2D array
 T1(ww,ii) = T(ww,jj,j);

 end

end
end
T(:,1,j+1) = T(:,40,j); % transfer the values of the last time step
 towards the next layer time step 1
end

t = 1:1:408*25; %Plot of the 2D aaray
plot(t,T1);
xlabel('Time (s)')
ylabel('Temperature C')
hold on
```

Published with MATLAB® R2018b

Vita

Xavier obtained a high diploma from Logos Academy located in Guayaquil, Ecuador. He earned a Bachelor of Science Degree in Mechanical Engineering from The Pennsylvania State University in May of 2017. As an undergraduate student, Xavier conducted research with Dr. Tim Simpson related to the effect that 3D printing has on air quality. While pursuing his undergraduate degree Xavier was part of the Alpha Fire Company and the University Ambulance Service where he volunteered countless hours to serve his community.

At the University of Texas at El Paso, Xavier conducted research under the guidance of Dr. David Espalin focused in large- and small-scale hybrid material extrusion additive manufacturing systems. Besides the work outlined in this thesis, Xavier developed the controls for an in-house build custom hybrid material extrusion 3D printer. He also updated the controls for a larger custom industrial material extrusion 3D printer.

Xavier will start his Doctoral degree at the University of Pittsburgh focused in wire arc additive manufacturing in the Fall of 2019 under the guidance of Dr. Albert To.